Crustal Block Rotations and Plate Coupling

Robert McCaffrey

Department of Earth and Environmental Sciences, Rensselaer Polytechnic Institute, Troy NY

Partitioning of slip at oblique subduction zones is common and frequently results in lithospheric blocks being detached from the overriding plate. A method is described to solve simultaneously for both block rotations on a sphere and locking on block-bounding faults using GPS vectors and other geophysical data. Example cases from Sumatra, Oregon, and Costa Rica, where mobile blocks are suspected, show that considering both block rotations and fault locking significantly improves the fit to the data over models that consider only one of them.

INTRODUCTION

The use of the Global Positioning System (GPS) to measure crustal deformation has added a new dimension to understanding the plate kinematics and deformation arising from plate interactions. Prior to the advent of GPS, geodetic measurements could unambiguously provide strain rates and uplift rates, but motions of rigid, rotating blocks of the lithosphere were not easily measurable. However, such motions add a complexity to the velocity fields measured with GPS particularly when strain rates within the blocks due to locking across block-bounding faults are significant.

The detachment of forearc blocks from the overriding plate in cases of oblique convergence has been documented for quite some time [*Fitch*, 1972; *Jarrard*, 1986]. From analysis of the deviations of subduction zone earthquake slip vectors from their directions predicted by plate motions, *McCaffrey* [1996] showed that about half of all modern subduction zones have mobile forearc blocks. The motion of a forearc block has two important impacts on a region's surface velocity field. First, the motion itself causes points in the forearc to move (rotate) relative to the rest of the overriding plate and if this rotation is about a nearby axis, it produces measurable horizontal gradients in the block's velocities. Second, the motion of the forearc changes the direction and rate of convergence at the subduction zone because such convergence is no longer between the large, upper plate and the subducting plate but instead is between the detached forearc and the subducting plate (Fig. 1a). In subduction zones, strain rates within the forearc commonly arising from coupling between the plates will reflect the new convergence vector. The surface velocities arising from these two factors are directly related but can interact in non-intuitive ways.

In this paper I outline a general method to model both the block rotations and the strain rates produced by locking on

block-bounding faults and apply it to oblique convergent margins. I discuss aspects of the effects of plate coupling and block rotation and suggest strategies for interpreting the complex velocity fields. I also present examples from three oblique convergent margins – Sumatra, Oregon, and Costa Rica - in which motions of forearc blocks are evident in GPS results. Here the method is applied to forearc blocks but is general and can be applied to other situations where multiple crustal blocks move relative to one another and are strained near their boundaries.

This approach has some history. *Matsu'ura et al.* [1986] modeled translating crustal blocks in a Cartesian coordinate system strained at their edges by fault interactions but did not include rotations. *Prawirodirdjo et al*. [1997], using my computer program DEF-NODE [*McCaffrey*, 1995], modeled the three-plate problem of slip partitioning in Sumatra using spherical Euler poles to describe both the kinematics of block motions and the relative slip on block-bounding faults. Backslip was applied to estimate the contribution of fault locking to the total velocity field. (*Murray and Segall* [2001] recently claimed credit for this approach but as I show in the Appendix, we have been doing it for several years.) *Meade and Hager* [1999] and *McCluskey et al*. [2001] inverted for Cartesian translations and rotations of crustal blocks. *McCaffrey et al.* [2000] and *Savage et al.* [2000] used geodetic data from Oregon to invert for both block rotations on a sphere (using Euler poles) and locking on the Cascadia thrust fault.

VELOCITY FIELDS, ROTATION, AND STRAIN

To understand the interaction of rotations and strain rates in a velocity field, I briefly review the decomposition of the horizontal surface velocity field. In practice horizontal is defined in two ways: (1) the *xy* plane in a Cartesian coordinate system - all velocity vectors are parallel to the *xy* plane,

$$\mathbf{V}(x,y) = (V_x(x,y), V_y(x,y))$$

and (2) the local tangent to the surface in a spherical or ellipsoidal coordinate system - all the velocity vectors are tangent to the surface,

$$\mathbf{V}(\lambda, \phi) = (V_e(\lambda,\phi), V_n(\lambda,\phi))$$

where λ is latitude, ϕ is longitude, and locally *e* is east and *n* is north. GPS vectors are commonly reported in an ellipsoidal coordinate system while some analyses, such as deformation modeling, are done in Cartesian coordinates and a transformation is necessary. Quite often we assume that $V_x = V_e$ and $V_y = V_n$ and geodetic station positions are converted to Cartesian coordinates using a Universal Transverse Mercator projection [*Snyder,* 1985]. These transformations produce little distortion unless the region of interest is very large.

In a Cartesian coordinate system, the velocity field can be used to form the velocity gradient tensor **L** from which rotation and strain rates are estimated. To estimate uniform, two-dimensional (surface) infinitesimal strain and rotation rate tensors from the horizontal components (x=east, y=north) of the estimated GPS-derived velocities, the velocity field $\mathbf{V}(x,y)$ is decomposed as follows:

$$\mathbf{V}(x,y) = \mathbf{L}\,\mathbf{X} + \mathbf{T} + \mathbf{E}(\mathrm{X})$$

where

$$\mathbf{L} = \begin{vmatrix} \partial V_x/\partial x & \partial V_x/\partial y \\ \partial V_y/\partial x & \partial V_y/\partial y \end{vmatrix},$$

X is a position vector, **T** is a position independent translation vector (T_x, T_y), and **E**(**X**) is a position-dependent error vector field. Written out in its components the velocity field in Cartesian coordinates is

$$V_x(x, y) = (\partial V_x/\partial \mathrm{x})\ x + (\partial V_x/\partial \mathrm{y})\ y + T_x + E_x(x, y) \quad (1a)$$

$$V_y(x, y) = (\partial V_y/\partial \mathrm{x})\ x + (\partial V_y/\partial \mathrm{y})\ y + T_y + E_y(x, y) \quad (1b)$$

Using the observed values of V_x and V_y from the GPS observations, the components of **L** and **T** can be estimated by weighted least squares. The estimated correlations between the horizontal velocity components are often small (<0.1) and could be ignored although it is a simple matter to solve equations 1a and 1b simultaneously while using the covariances between components. If the uncertainties are properly scaled and the deformation is indeed uniform, the overall χ^2 misfit should roughly equal the number of degrees of freedom.

The velocity gradient tensor is the sum of the strain rate and the rotation rate tensors: $\mathbf{L} = \boldsymbol{\varepsilon} + \boldsymbol{\theta}$. The strain rate tensor $\boldsymbol{\varepsilon}_{ij} = \frac{1}{2}\,[\,\partial V_i/\partial x_j + \partial V_j/\partial x_i\,]$, i =1,2 and the rotation rate tensor is $\boldsymbol{\theta}_{ij} = \frac{1}{2}\,(\partial V_i/\partial x_j - \partial V_j/\partial x_i)$, where $x_1 = x$ and $x_2 = y$. The magnitudes and directions of the principal strain rates are estimated by finding a coordinate system that zeroes the off-diagonal elements of the strain rate tensor. *Savage et al.* [2001] give the formulation for estimating strain and rotation rates in a spherical coordinate system. The spherical solution gives insignificantly different results compared to the Cartesian approximation for networks that are several hundred kilometers in aperture (*J. Savage* pers. comm., 2001).

BLOCK ROTATIONS AND FAULT LOCKING STRAIN

Like the motions of large tectonic plates, the motions of smaller blocks on the surface of the Earth can be described by rotations about vertical axes, often called Euler poles,

that intersect the center of the Earth. To the eye these rotations produce gradients in the surface velocity field that could be mistaken for shear strain rates because both involve the components dV_x/dy and dV_y/dx of the velocity gradient tensor.

The magnitude of the velocity of a point on the Earth's surface due to rotation about an Euler pole is $\omega R_e \sin \Delta$, where ω is the angular velocity, R_e is the radius of the Earth and Δ is the angular distance of the point from the pole. The gradient in the transverse velocity along a small circle is $\omega R_e \cos \Delta$ which approaches zero as Δ approaches 90°. Hence, a small block rotating about a distant axis has small velocity gradients and the rotations can sometimes be treated as translations (*i.e.*, the V_n and V_e components are approximately both independent of position). Distant poles of rotation are often implicitly assumed in discussions of forearc sliver motions and this has led to the notion that forearc slivers 'translate' along the margin, that is, that the velocity vectors are uniform throughout them. In considering large blocks or those that are close to their pole of rotation, the velocity gradients due to rotation must be properly modeled.

Many observed GPS velocity fields can be explained by rigid rotating blocks that are strained near their edges due to interactions with other blocks across the bounding faults (Fig. 1a). Here I describe an approach to combine block rotations with the commonly used half-space dislocation models that describe strain near locked faults. For the blocks, rotation poles describe both the rigid block motions and the long-term average relative slip across the block-bounding faults. Dislocation modeling is then used to estimate velocity perturbations within the blocks due to locking on the bounding faults and these velocities are added to the rotational velocities. In the case of a single mobile forearc block, as depicted in Fig. 1a, the model domain comprises three blocks separated by two faults. Because plate locking strain typically extends hundreds of kilometers landward from the coast at subduction zones, in general the rotation pole for a forearc block and plate locking parameters cannot be estimated independently for small forearc blocks. Accordingly, I use a simultaneous inversion for block rotation and fault locking.

The motion of each block is described either by a Euler pole in spherical coordinates or by a local Cartesian rotation about a vertical axis. In most applications some poles are specified and others are estimated. However, it is possible to estimate all poles, which might be desirable, for example, when the reference frame for the GPS solution is not independently tied to a specific block (*e.g.*, all poles could be in an ITRF frame). An Euler pole may not be a suitable parameterization when it is far from the block, in which case it is poorly constrained. Alternatively, rotations about a vertical axis are described by the horizontal velocity at a specified point in the block and a rotation rate [*Meade and Hager*, 1999].

An Euler pole in a spherical coordinate system ${}_R\mathbf{\Omega}_i = (\lambda_p, \phi_p, \omega)$ gives the rotation of point (λ, ϕ) in block *i* in the reference frame R, where R can be another plate or reference system such as no-net rotation (NNR) or a GPS reference frame (*e.g.*, ITRF96). The linear, horizontal velocity of a point within block *i* relative to reference frame R is ${}_R\mathbf{V}_i = {}_R\mathbf{\Omega}_i \times \mathbf{X}$ where $\mathbf{X}$ is the vector pointing from the center of the Earth to the surface point (λ, ϕ) at which the velocity is to be estimated. For small blocks one can alternatively represent rigid rotation by specifying or estimating the linear velocity $\mathbf{V}_o$ (x_o, y_o) at an arbitrary point (x_o, y_o) within the block plus a local, vertical axis rotation rate ω':

$$V_x(x, y) = V_{xo}(x_o, y_o) - \omega' (y - y_o)$$

$$V_y(x, y) = V_{yo}(x_o, y_o) + \omega' (x - x_o) \qquad (2)$$

It can be shown that the local vertical axis rotation rate is related to the Euler rotation rate by: $\omega' = \omega \cos \Delta$.

The long-term slip velocity across a block-bounding fault is the difference in the linear velocities of the two blocks, calculated from the Euler poles at the point of interest on the fault. The slip velocity on a fault that separates blocks *i* and *j* at point $\mathbf{X}$ is:

$${}_j\mathbf{V}_i = {}_R\mathbf{V}_i - {}_R\mathbf{V}_j \qquad (3)$$

Some part of this relative slip rate on the fault does not occur steadily and we refer to this as 'locking' of the fault. Such locking results in strain rates within the blocks. Velocity perturbations due to locking are calculated and added to the rotational velocities. I apply the *Savage* [1983] backslip method using the formulas of *Okada* [1985] to compute surface velocities around locked faults embedded in a homogeneous, elastic half-space. Because the velocities due to Euler rotations are calculated in spherical coordinates and plate locking velocities are typically calculated in Cartesian coordinates, as above, I assume that $V_x = V_e$ and $V_y = V_n$. It should be noted that the surface deformation due to the fault interactions can be calculated with any appropriate method and the material need not be fully elastic. For example, we are also using elastic 'plate' models in lieu of halfspace models [*Williams et al.*, 2001].

Like many others, I describe fault locking as the fractional part of relative plate motion that is not accommodated by steady, aseismic slip and call the parameter ϕ the spatially averaged fraction of the fault area that is stuck (ϕ ranges from 0 to 1). To parameterize plate locking on an irregular fault surface, I specify nodes along contours of the faults (Fig. 2a) and in the inversion solve for the value of ϕ at them. The fault slip vector $\boldsymbol{V}$ at a node is the long-term slip rate vector across the fault due to the relative motions of the adjacent blocks (equation 3). The use of rotation poles to calculate the fault slip for the deformation model greatly simplifies calculations of relative plate motions across the

faults and assures that the block model is kinematically self-consistent. For example, along-strike forearc migration makes the convergence direction at trench less oblique - by using poles the new direction is automatically used. Plate locking is then represented by applying backslip on the fault at a rate of $-\phi\boldsymbol{V}$ (the product $\phi\boldsymbol{V}$ is also sometimes called 'slip deficit' because it represents the amount of the expected long-term slip rate on the fault that is not taken up by steady creep). In this implementation, all slip is constrained to be in the plane of the fault.

For numerical purposes, each node is thought of as being at the peak of an irregular pyramidical weighting function and thus represents a weighted average of $\phi\boldsymbol{V}$ over the area enclosed by the eight adjacent nodes (Figs. 2b and 2c). The pyramidical weighting function decays linearly to zero at each of the adjacent nodes. (A bilinear weighting function, which gives a curved decay across diagonals of the elements, gives nearly identical results.) The contribution to the surface velocities from each node is calculated by integrating slip rates over the area between the node and the eight adjacent nodes. To integrate, the area is divided into small patches and $\phi\boldsymbol{V}$ is estimated for each patch using the pyramidical weighting function. The surface velocity due to slip on each patch is estimated and these are all summed. The patches are typically only a few kilometers on a side and can be larger for deeper parts of the fault. The practice of specifying nodes along depth contours assures that the quadrilateral enclosed by four adjacent nodes (two at each depth contour) is a planar trapezoid. During integration over the fault the subregions are also trapezoids and do not necessarily form rectangles as are used in the *Okada* [1985] finite source formulation. However, as the subregions are made smaller their actual shape becomes unimportant – they approach a point source so only their area, orientation, and centroid location are needed for an accurate estimate.

Because the downhill simplex method used to find the best fitting set of parameters requires many solutions to the forward problem, I first generate response functions at each observation point for each node. The response functions are the velocities observed at the surface observation point caused by unit velocities both along-strike and downdip at the node. Once these unit responses are calculated by integration as described above, the surface velocities due to a specific slip rate distribution on the fault are found by the relatively fast summation of the response functions, each of which is scaled by the slip rate ϕV at its corresponding node. These unit response functions can also serve as derivatives in inversions that require them.

In inversions for interseismic plate coupling, ϕ is kept between 0 and 1 to prevent reverse subduction or locking at a rate faster than plate convergence by applying a penalty function. In the case studies, I fix $\phi = 0$ at the deepest nodes on each fault, noting that seismicity, and presumably fault locking, ceases at depth. This constraint forces the coupling to taper to zero at the downdip end of the fault. Because it

is questionable whether or not halfspace dislocation models correctly represent a downdip increase in coupling, I can impose a monotonic downdip decrease in ϕ by constraining each ϕ to be less than or equal to ϕ at the node directly updip from it. This imposes a smooth transition from locked to unlocked in the downdip direction but does not specify the form or width of this transition.

Gradients at lateral fault edges are minimized by placing nodes on the faults outside the geodetic network and forcing them to have the same values of ϕ as adjacent nodes at the edges of the network (as is done using 'fictitious' nodes in finite difference methods to remove gradients at the model edges). To increase the sensitivity of the data for the estimated fault locking parameters, multiple contiguous nodes can be grouped to form a single free parameter. Grouping increases the area of the fault covered by a single free ϕ parameter which decreases the uncertainty in that ϕ but at the expense of spatial resolution. For example, because land geodetic observations are largely insensitive to the near-trench locking, trench nodes are usually forced to have the same ϕ as adjacent nodes downdip. Other nodes can be grouped based on the parameter covariance from test runs in which all nodes are free and independent.

The observation misfit function to be minimized is the reduced chi-square, $\chi_v^2 = (n - P)^{-1} \Sigma_{i=1,n} (r_i / f\sigma_i)^2$ where n is the number of observations, P is the number of free parameters in the inversion, r_i is the residual (the observed minus calculated data), σ_i is the formal data uncertainty, and f is a data uncertainty scaling factor. The scaling factor is used to balance the influence of the various data types and to account for additional uncertainties not included in the formal data uncertainty estimates. For example, formal GPS velocity uncertainties are typically underestimated by a factor of 2 to 5 [*Mao et al.*, 1999]. To find a set of parameters that minimizes χ_v^2, I apply simulated annealing to downhill simplex minimization [*Press et al.*, 1989]. At the minimum χ_v^2, the parameter covariance matrix is estimated by singular value decomposition of linearized normal equations.

Currently, to constrain the locking distributions and rotation poles I use horizontal GPS velocities, surface uplift rates (GPS, tide gauge, or leveling), surface tilt rates, earthquake slip vectors, fault slip rates, and transform fault azimuths. Surface velocities are given by:

$$V_i(\mathbf{X}) = \sum_{b=1,B} H(\mathbf{X} \in \triangle_b) [{}_R\boldsymbol{\Omega}_b \times \mathbf{X}] \cdot \hat{\imath} -$$

$$\sum_{k=1,F} \sum_{n=1,Nk} \sum_{j=1,2} \phi_{nk} G_{ij}(\mathbf{X}, \mathbf{X}_{nk}) [{}_h\boldsymbol{\Omega}_f \times \mathbf{X}_{nk}] \cdot \hat{\jmath}$$

where:
$\mathbf{X}$ is the position of the surface observation point,
B is the number of blocks,
$\triangle_b$ is the subset of the model domain within block b,
$H = 1$ if the point $\mathbf{X}$ is contained within block b, $H = 0$ otherwise,

i index for velocity component (x, y, or z),
$\hat{\imath}$ is the unit vector in i direction,
${}_R\boldsymbol{\Omega}_b$ is the Euler pole of block b relative to the reference frame,
${}_h\boldsymbol{\Omega}_f = {}_h\boldsymbol{\Omega}_R - {}_f\boldsymbol{\Omega}_R$ is the Euler pole of the footwall block f of fault relative to the hangingwall block h,
F is the number of faults,
N_k is the number of nodes defining fault k,
$\mathbf{X}_{nk}$ is the position of node n on fault k,
ϕ_{nk} is the coupling fraction at node n on fault k,
$\hat{\jmath}$ is the unit vector in j^{th} direction on fault surface (downdip or along strike), and
G_{ij} ($\mathbf{X}$, $\mathbf{X}_{nk}$) is the response function giving the i^{th} component of velocity at surface point $\mathbf{X}$ due to a unit slip velocity along fault surface at node $\mathbf{X}_{nk}$ in the j^{th} direction.

The first term is the block rotation and is applied for all points on a block using its rotation pole. The second term is the fault locking (backslip) term where the backslip velocity is taken from the Euler poles and then multiplied by the coupling fraction to get the slip deficit on the fault. The slip deficit at the node is then multiplied by the response function G to get the surface velocities. G is the surface response to the pyramidical slip distribution. Equation 2 can be used in lieu of the cross-products to estimate velocities when using vertical axis rotations.

Surface tilt rates are given by the finite difference:

$$T(\mathbf{X}) = [\, V_z(\mathbf{X}+\Delta\mathbf{X}) - V_z(\mathbf{X} - \Delta\mathbf{X}) \,] / (2\,|\Delta\mathbf{X}|\,)$$

where $\mathbf{X}$ is at the mid-point of the leveling line and $\Delta\mathbf{X}$ is the offset from the mid-point to the ends. Slip vector and transform fault azimuths are given by the azimuth of slip along the fault between two adjacent blocks:

$$A(\mathbf{X}) = \arctan\{\, [\, {}_h\boldsymbol{\Omega}_f \times \mathbf{X} \,]_n / [\, {}_h\boldsymbol{\Omega}_f \times \mathbf{X} \,]_e \,\}$$

where the subscripts e and n represent the east and north components, respectively. Geologically estimated fault slip rates or spreading rates are:

$$R(\mathbf{X}) = |\, {}_h\boldsymbol{\Omega}_f \times \mathbf{X} \,| = |\, {}_h\mathbf{V}_R - {}_f\mathbf{V}_R \,|$$

OBLIQUE CONVERGENCE AND SLIP OBLIQUITY

Using this approach I first look at some simple examples of velocity fields for forearc blocks that are being strained by plate coupling and also moving relative to the overriding plate. Figure 3 shows hypothetical examples of surface velocities, obliquity, and principle strain rates across a subduction margin with varying degrees of both plate coupling on the subduction fault and forearc motion. The reference frame is the overriding plate far from the plate boundary (Fig. 1b). These examples were derived using a halfspace

dislocation model based on the formulas of *Okada* [1985]. The rotation pole for plate S relative to plate O was chosen such that the subducting plate to the left of the trench (at x = 0) converges at an angle (obliquity) of $\varphi = 45°$ relative to the trench normal and plunges below the overriding plate at 10° dip angle. The coupling between the two plates is estimated by applying backslip at the same rate as plate convergence but in the opposite direction [*Savage*, 1983]. In each case the fault is presumed to be fully locked from the surface down to the nominal coupling depth (DC) and then locking decreases linearly to zero over the next 10 km of depth. The slip partitioning (SP), the fraction of the along-strike component of relative motion that is assumed to be taken up by a strike-slip fault within the overriding plate, is tested at 0%, 50%, and 100%. The strike-slip fault in these tests is placed at 300 km from the trench and is fully locked from the surface down to 15 km depth (*i.e.*, backslip is applied on the strike-slip fault as well). Its slip vector is specified by a pole between plate F and plate O. The relative convergence direction between the subducting plate and the forearc is corrected to account for the motion of the forearc (Fig. 1b) simply by summing the poles ${}_F\mathbf{\Omega}_S = {}_F\mathbf{\Omega}_O + {}_O\mathbf{\Omega}_S$. Hence, the obliquity of convergence between the subducting plate (S) and the forearc (F), the obliquity that is measured with subduction slip vectors and referred to as γ (Fig. 1b), is 45° for SP = 0, 22.5° for SP = 50%, and 0° for SP = 100% while the obliquity of the convergence between the subducting plate and the upper plate beyond the strike-slip fault (Plate O) is 45° for all cases. From here on, I refer to obliquity in the reference frame of the overriding plate beyond the strike-slip fault and not in the reference frame of the forearc. The obliquity of the surface velocities is represented by φ' in Figure 1b.

In the case where there is no margin-parallel strike-slip fault (Fig. 3, top row, SP = 0%), the horizontal surface velocities on the hanging wall but near the trench show the same obliquity as the relative plate convergence vector. Over the downdip edge of the coupled zone (shown by short, thick line) there is a slight increase in the obliquity and inland of this point the vectors decrease in magnitude and rotate to become more normal to the trench (obliquity gradually decreases). The decrease in obliquity landward of the DC is caused by elevation in the margin-parallel shear strain rate over the downdip end of the coupled zone [*Savage*, 1983]. The small, more localized increase in the obliquity over the DC in these cases appears to be caused by kinks in the modeled plate locking distribution. Tests that use less abrupt downdip transitions from locked to unlocked reveal smaller increases in obliquity above the DC (Fig. 4).

In cases where a large fraction of the margin-parallel relative motion is taken up by motion of the forearc (2nd and 3rd rows of Fig. 3), the surface velocities landward of the coupled zone rotate to become more parallel to the margin, that is, more oblique than the convergence direction. This

rotation of the vectors occurs because the trench-normal component of the velocities decays rapidly landward while the trench-parallel component (due to forearc motion) does so more slowly. In other words, during slip partitioning the strike-slip fault and not the dipping thrust fault controls where the shear strain in the overriding plate is concentrated. Note that the surface velocities at the trench are parallel to convergence (e.g., obliquity is 45°) and remain so for some distance landward of the trench. Because subduction zone trenches are typically 100 km or more from the nearest land, in most cases where forearc motion occurs, GPS vectors near the coast are expected to be more oblique than the plate convergence vector. Hence, a first-order indicator of slip partitioning is that the GPS vectors at sites inboard from the trench are more parallel to the margin than is the expected plate convergence vector. However, GPS obliquity does not always reveal slip partitioning. A situation in which block motion does not produce an appreciable increase in GPS obliquity is when the downdip end of coupling and the strike-slip fault are geographically close (examples in Fig. 3 are cases where DC = 30 km and SP = 50% and 100%).

The presence or absence of forearc block motion can also be revealed by looking at the principal strain rates (Fig. 3). When block motion does not occur, the principal strain rate axes over the DC are oriented obliquely relative to the plate margin. When block motion occurs the shear strain steps back to strike-slip fault (or some other type of fault separating the block from the rest of the overriding plate) and the strain in the forearc is uniaxial contraction more normal to the margin [*Savage and Lisowski*, 1988]. Hence, in the case of oblique convergence, slip partitioning is revealed by the principal contraction rate at the leading edge of the hanging wall being nearly normal to the margin.

In contrast to the results presented here, *Bevis and Martel* [2001] suggest that the obliquity of the surface velocities can get up to twice the plate convergence obliquity even in the absence of sliver motion. I disagree with their results on the grounds that the particular implementation of the elastic half-space dislocation model upon which they base their conclusions is incorrect. Their inclusion of a 'free-slip' zone on the thrust fault seaward and updip of a deeper locked zone results in improbable strain rates in the wedge above it and these strain rates are nearly entirely responsible for their inference of a large obliquity anomaly (Fig. 4).

To understand why their inference of large strain rates in the wedge above the updip free-slip part of the thrust fault is incorrect, consider a balance of the margin-parallel forces acting on this wedge (Figs. 4a and b). The backslip concept proposed by *Savage* [1983] comprises the superposition of two solutions - one for the steady aseismic slip along the fault that leads to block-like motions (and a static stress field) plus a solution for the time-dependent deformation due to the growth of an edge dislocation [*Savage*, 1996]. Because we measure strain rates and not complete strain with geodetic techniques, our data are sensitive only to the

time-dependent part of the problem and we often ignore the static component (nevertheless, the block-like plate motions that give rise to the static stresses are included in the velocity field). Therefore, the time-dependent stress changes inferred by the elastic half-space dislocation (EHSD) model must satisfy a force balance. Simply put, I argue that the elastic wedge (wedge abc in Fig. 4b) overlying the updip free-slip zone included in the *Bevis and Martel* [2001] model is free of margin-parallel horizontal shear stress rates. Because two of its sides (ab and ac) are specified to be stress-rate free, the third side (bc) must also be stress-rate free. Hence, it must be free of margin-parallel shear strain rates.

Platt [1993] examined the deformation within a forearc wedge under oblique convergence starting from force balance equations. The horizontal force-balance in the strike-parallel direction for an infinitely long (two-dimensional) wedge is:

$$\partial\sigma_{xy}/\partial x + \partial\sigma_{yz}/\partial z = 0$$

(where x is across strike, y is along strike, and z vertical). This equation must hold whether σ represents stress or stress rates - here it refers to stress rates. If there is no basal traction rate (along segment ac in Fig. 4b) and the top of the wedge (segment ab in Fig. 4b) is a free surface, then $\partial\sigma_{yz}/\partial z = 0$, leaving $\partial\sigma_{xy}/\partial x = 0$ which has the solutions of either $\sigma_{xy}(x) = 0$ or $\sigma_{xy}(x) =$ constant. We can rule out the latter by using the relationship derived by *Platt* [1993]:

$$\sigma'_{xy}\,\theta / h - \partial\sigma'_{xy}/\partial x = 0$$

where σ'_{xy} is the vertically averaged horizontal shear stress rate on a vertical plane parallel to strike, θ is the taper of the wedge (angle between upper and lower wedge surfaces), and h is the local thickness of the wedge (in this case the basal traction rate is set to zero). This equation relates the stress rate gradients due to the taper of the wedge (1st term on lhs) and stress rate gradients from other sources. A constant vertically averaged stress rate does not satisfy this equation unless that constant is zero. Hence a two-dimensional wedge without margin-parallel basal traction rate is stress-rate-free. Its internal deformation rate is zero but it will move along strike at the same rate as the part of the upper plate directly above the updip end of plate coupling because there should be no across-strike gradients in its margin parallel velocity (*i.e.*, $\partial V_y/\partial x = 0$, this follows from the result that horizontal shear stress rates across the vertical plane bc in Fig. 4b are zero). Tests with finite element models that include force balance constraints reveal that the leading wedge of an elastic overriding plate does indeed move along strike as a coherent block even when the basal stress increases downdip [*McCaffrey et al*., 2000a].

Savage [1996] notes that the dislocation models were intended only to "approximate deformation associated with

aseismic slip on the plate interface downdip from the locked segment". A first-order attempt to represent an updip 'unlocked' segment is to lock it at the same rate as the updip end of the 'locked' zone. This forces the wedge to move with the overriding plate at about the same rate as the section over the updip end of the locked zone (this approach does not completely remove shear strain rates from the wedge as seen in Figs. 4d and e). While this approximation forces the deformation field to be more in agreement with what one infers from force balance arguments, it also implies that one cannot learn about the seaward (updip) extent of plate locking at a subduction zone from geodetic data alone. In other words, a paradox arises in that to model an 'unlocked' updip zone approximately correctly, one has to 'lock' that section of the fault in conventional elastic half-space dislocation models.

CASE STUDIES

Here I present three examples of applying the method described above to subduction zones where 'forearc' blocks are thought to be moving relative to the rest of the overriding plate. The term forearc block is used to refer to the detached crustal entity even though it sometimes includes part of the backarc region. For each region, I show results of inversions for spatially variable plate locking only where ϕ can vary along strike and downdip (VL), block rotation only (R), block rotation and uniform plate locking (UL-R; UL means ϕ is uniform on fault), and finally block rotation and variable locking (VL-R) (Table 1). For each trial I compute the misfit to the collective data, described by χ_v^2, and the misfit to the individual data types (Table 1), described by

$$\chi_{obs}^2 = n^{-1} \Sigma_{i=1,n} (r_i / f\sigma_i)^2$$

where n is the number of observations of that type, r_i is the residual, σ_i is the formal data uncertainty, and f is an uncertainty scaling factor as described earlier. The data types used are horizontal surface GPS velocity vectors (GPS in Table 1), earthquake slip vectors and transform fault azimuths (Az in Table 1), and uplift rates (Up in Table 1). The inversions reveal information on how the data are sensitive or not to plate locking and rotations. F-tests are used to see if the data fit is significantly improved or not by changing the numbers or types of parameters.

The three examples comprise: (1) Sumatra where the forearc is moving rapidly about a distant pole and separated from the overriding plate by a clear strike-slip fault, (2) Oregon where the forearc and arc are rotating about a nearby pole but the boundary of the rotating block with the overriding plate (North America) is not obvious, and (3) Costa Rica where the motion of the forearc is slow compared to the rate of subduction. The analyses presented are meant to be brief and illustrative – details of the interpretations of each region are left to other papers. Other examples

where GPS and other data have been used to constrain block rotation and fault strain are Asia [*Meade and Hager,* 1999], California [*McCluskey et al.* 2001], Sulawesi [*Stevens et al.,* 1999], Tibet [*McCaffrey*, 1999], and Papua New Guinea [*Wallace et al*., 2001].

Sumatra

The independent motion of the Sumatra forearc was first noted by *Fitch* [1972] and remains the classic example of the slip partitioning process. Based on the NUVEL-1a pole [*DeMets et al*., 1994], the direction of convergence of the Australian plate with the Eurasian margin SW of Sumatra is at about N18°E (Fig. 5a), giving obliquity that ranges from about 35° to 50° relative to the normal to the Java trench. The convergence rate of about 65 mm/a corresponds to about 43 to 55 mm/a of convergence normal to the trench and about 38 to 49 mm/a of slip parallel to the margin.

From 1989 to 1994 the author was part of a collaborative project with Scripps Institution of Oceanography and the Indonesian mapping agency BAKOSURTANAL to obtain GPS measurements from the forearc, arc, and backarc regions in Sumatra [*Prawirodirdjo et al*., 1997; *Genrich et al*., 2000]. The results serve to exemplify the expected velocity and strain fields when slip partitioning occurs. Here, I use the GPS vectors listed by *Genrich et al.* [2000] but modify them using the *Sillard et al*. [1998] Eurasia-ITRF96 pole to put them into the Eurasian reference frame rather than the Eurasia – No Net Rotation pole used by *Genrich et al.* [2000].

In margin-normal profiles of the GPS vector obliquities, it is evident that vectors from the southern forearc sites move with approximately the same obliquity as the relative plate convergence and then become more margin-normal in the backarc (Fig. 6). In contrast, northern forearc velocities show obliquities that are systematically larger than relative plate convergence obliquity. Although there is considerable scatter, the obliquities appear to increase landward away from the trench, reach a maximum in the forearc, and then decrease across the Sumatra fault. This northern obliquity profile resembles the cases for shallow interplate coupling and forearc motion shown in Figure 3 (for examples, SP = 50% or 100% and DC= 10 or 20 km). The southern profile, which shows a flatter obliquity curve, could be interpreted as indicating either no slip partitioning or slip partitioning with strong coupling (for example, DC = 30 profiles in Fig. 3). The principal contraction rates in the forearc are approximately normal to the trench and the strain rates become more margin-parallel shear near the arc, indicative of partitioning (Fig. 5a; Table 2). Hence, the GPS results from both the north and south halves of the GPS network in Sumatra resemble the highly partitioned cases shown in Fig. 3.

In *Prawirodirdjo et al*. [1997], we explained the along-strike variation in the Sumatra GPS results by forward modeling a combination of plate locking and rigid rotation of the Sumatra forearc. In that paper, we assumed a rotation

pole for the forearc motion relative to Eurasia whose location was based on a least-squares small-circle fit to the Sumatra fault and whose angular velocity predicted about 28 mm/a slip on the Sumatra fault (pole at 12°N, 117°E, and ω = -0.7 °/Ma). The Sumatra fault (SF) was assumed to be locked to 15 km depth (backslip was applied to the upper 15 km of the boundary between the forearc and Eurasia).

Here, I perform inversions to estimate the pole of rotation for the forearc's motion while simultaneously solving for the locking on the subduction plate boundary and the Sumatra fault. In addition to horizontal GPS vectors, I utilize earthquake slip vectors (Fig. 5b; Table 1) that constrain the direction of relative motion between the forearc and the Australian plate, azimuths of the SF that constrain the direction of motion of the forearc relative to Eurasia, and coral uplift rates of the forearc islands from *Sieh et al*. [1999] that locally constrain plate coupling. Slip vectors and fault azimuths are all given a standard error of 15° for the purposes of weighting in the inversion. Uplift rates were assigned five times the uncertainties quoted by *Sieh et al*. [1999] and the formal GPS vector uncertainties were doubled. The relative weighting controls the influence each data type has on the final solution. The small quoted errors in the coral uplift rates caused these observations to be dominant in the inversion and they were subsequently increased to allow the GPS and slip vectors to be fit better.

The model comprises the subducting Australian plate, the forearc and the overriding Eurasian plate. The motion of the Australian plate relative to Eurasia is given by the NUVEL-1A pole [*DeMets et al*., 1994]. The forearc block is separated from the Eurasian plate along the SF and from the Australian plate along the subduction thrust. Along the thrust fault nodes were placed at depths of 5, 13, 25, 50, 75, and 100 km and at 0, 15, and 20 km on the SF (Fig. 7). The deepest nodes on both faults were forced to be uncoupled (ϕ = 0). In the variable coupling models, nodes on the thrust fault were allowed to vary along strike and at the edges of the faults the two end nodes were held the same. Because the nodes at the trench are poorly constrained in such inversions, they were forced to have the same value as those immediately downdip from them at 13 km depth. The 42 nodes on the thrust fault shown in Fig. 7 form 14 free parameters in the variable locking inversions. Sumatra fault nodes were all constrained to have the same locking in all inversions (1 free parameter). In addition, 3 parameters are used to represent the rotation of the forearc relative to Eurasia.

The impact of using rotation and plate locking simultaneously was examined by performing inversions allowing only one or the other and then both together (Table 1). For Sumatra, variable plate locking alone (χ_ν^2 = 4.42) appears to explain more of the observations than does rotation alone (χ_ν^2 = 7.43). This may occur because the forearc sites, in the absence of coupling on the Sumatra fault, are the only ones affected by forearc rotation but are few and have rela-

tively large uncertainties. The sites NE of the Sumatra fault are affected by forearc rotation only through coupling on the Sumatra fault. Assuming uniform locking and rotation provided a fit that is similar to the variable locking model ($\chi_\nu^2 = 4.55$; Table 1) but with much fewer free parameters.

A significantly better fit ($\chi_\nu^2 = 2.33$) was obtained by including both rotation and variable coupling (VL-R). F-tests indicate that this model fits the data better than the previous three models at >99.99% level (Table 1). The utility of including both locking and rotation shows up clearly in the fits to the azimuths (Table 1). Without forearc rotation, convergence at the Java trench is determined by the AUS-EUR rotation pole, which matches the slip vectors poorly ($\chi^2_{az} = 2.57$). Solving for rotation only (no plate coupling), the estimated pole of rotation is again incorrect because the inversion tries to find a pole to match the forearc GPS vectors that are 'contaminated' by plate coupling strain, leading to a poor match of the azimuths ($\chi^2_{az} = 2.91$). When both rotation and coupling are modeled (models UL-R and VL-R), a better pole is estimated and the slip vector azimuths are satisfied ($\chi^2_{az} \approx 1$).

The rotation pole for the forearc relative to Eurasia is near 24°N, 231°E, and a rotation rate of -0.15°/Ma, with very large uncertainties due to the small aperture of the observations. This pole predicts only 14 mm/a of slip on the Sumatra fault which is about half the estimates from GPS profiles across the fault [*Genrich et al*., 2000]. A better estimate of the forearc's motion is made by solving directly for the linear velocity at a point within it and its vertical axis rotation rate. The velocity at 0°N, 100°E, close to the Sumatra Fault, is 13.7 ± 6.9 mm/a to the WNW (Fig. 5b). The rotation rate about a nearby vertical axis is 0.08 °/Ma ≈ 1 nanoradian/a, and therefore contributes little to the velocity field. (The use of vertical axis rotation results in a slightly higher χ_ν^2 of 2.340 compared to 2.331 when using the Euler pole, presumably due to the flat-Earth approximation in the former approach.)

The discrepancy in SF slip rates may be explained in two ways. Geologic estimates of the long-term fault slip rate changes at about 1°N from 11 mm/a to the south to 22 mm/a north of 1°N (see *Genrich et al*. [2000] for sources of geologic rates). The estimate of the forearc motion in this study is based on GPS data extending from 3°S to 3°N and may sample an average of these rates. In other words, in this analysis I assume the forearc is rigid while other estimates of SF slip rates suggest it is not. Alternatively, or in addition, some part of the NW motion of the forearc evident in the GPS vectors may in fact be elastic strain due to the obliquity of the coupling on the thrust fault and not permanent deformation of the overriding plate.

The inversion VL-R_c was performed in which the forearc rotation pole was constrained to produce 28 mm/a slip rate on the Sumatra fault, as was assumed by *Prawirodirdjo et al*. [1997], resulting in $\chi_\nu^2 = 4.13$, a 0.03% probability of being as good a fit as the VL-R model. This inversion re-

sulted in greater locking on the Sumatra fault, 90% compared to 20% for the VL-R model which had a slower moving forearc block. Apparently the inversion attempted to slow the forearc's too-rapid motion in model VL-R_c by increasing locking on the Sumatra fault.

The most interesting result from the rotation and variable locking inversions is that the low-coupling zone that we thought included the entire northern half of the forearc [*Prawirodirdjo et al*., 1997] appears as a small patch from the equator to about 1°N (Fig. 7). The manifestation of this poorly-locked patch is the relatively low contractional strain rate in this section of the forearc (Fig. 5a; Table 2). This poorly-locked patch appears to be rubust because it is the only difference between models UL-R and VL-R; in the VL-R model the thrust boundary away from the poorly-locked region is uniformly fully locked. An F-test indicates that the UL-R model, that does not include the poorly-locked patch, has a probability of about 0.0027% of fitting the data as well as the VL-R model, that includes the patch.

The unlocked patch falls in the section of the forearc where the Investigator Fracture Zone (IFZ; Fig. 5a) subducts, suggesting a causal correlation. It was also noted by *Prawirodirdjo et al*. [1997] that the rupture zones of two great subduction thrust earthquakes in the 1800's [*Newcomb and McCann*, 1978] were truncated at about this latitude. The poorly-locked patch, possibly caused by the subduction of the IFZ, may form a barrier to earthquake rupture propagation along the Java trench.

Oregon

The Juan de Fuca plate converges obliquely with North America at about 40 mm/a along the southern half of the Cascadia subduction zone (Fig. 8). Rotation of the Oregon forearc relative to North America was recognized in the region's geology and paleomagnetic declinations by *Wells et al*. [1998] and in GPS by *Savage et al*. [2000] and *McCaffrey et al*. [2000b]. *McCaffrey et al*. [2000b] used horizontal vectors from 71 GPS sites in western Oregon and four tilt rates near the Oregon coast to solve simultaneously for plate locking and rotation of Oregon. Additional campaign measurements and re-processing now allow velocity estimates for 117 GPS sites (Fig. 8a). Site positions were calculated in the ITRF97 reference frame and velocities and their covariances were estimated by linear regressions to the time series. Velocities were put in the North American (NA) reference frame by removing NA-ITRF97 rotation [*Sella et al*., 2001]. The vectors shown in Figure 8 are based on more than 2 years of campaign observations. Seven uplift rates are estimated from tide gauge data. No slip vectors are available due to the lack of seismicity at the Cascadia thrust.

The GPS vectors from Oregon in the NA reference frame reveal a clear rotational pattern with an axis in northeastern Oregon (Fig. 8a). An indication that partitioning occurs is that the GPS vectors in coastal SW Oregon are more paral-

lel to the margin than is the Juan de Fuca – North America convergence vector (compare to Fig. 2). In fact, in inland SW Oregon the vectors point more westward than the trend of the margin indicating that the rotation of the forearc is about a nearby pole (examples in Fig. 2 are based on a distant pole).

As in Sumatra, the principal contractional strain rates are uniaxial and nearly normal to the deformation front in the forearc but, unlike Sumatra, they do not rotate significantly near the arc (Fig. 8a; Table 2). We see little evidence in the GPS results that the Oregon forearc is moving northward by localized shear along the volcanic arc [*Wells et al*., 1998] or in distributed shear zones [*Miller et al*., 2001]. Instead, strain rates largely reflect contraction of the upper plate by eastward subduction of the Juan de Fuca plate beneath western Oregon. Exceptions to this strain rate pattern are in south-central Oregon where there is more NW-directed uniaxial contraction (-28±8 nanostrain/a) and in south-central Washington there appears to be shear (left-lateral on NW-trending planes or right-lateral on NE-trending planes) although the rate of northerly extension there is not well resolved (27±20 nanostrain/a). Elsewhere along the arc and backarc the strain rates are relatively low, generally less than 10 nanostrain/a, roughly at about the level of their uncertainties. Hence, although we cannot rule out strain rates at the 10 nanostrain/a level arising from permanent deformation within Oregon, the majority of the GPS velocities relative to North America are explained by a rigid rotation of Oregon with superimposed strain rates due to the plate boundary coupling.

Using the same node distribution to represent the Cascadia thrust used by *McCaffrey et al*. [2000b] which was based on the *Hyndman and Wang* [1995] fault model, I invert the GPS vectors and uplift rates to solve for plate locking and rotation of western Oregon (Fig. 9). I use 8 nodes along strike and 6 downdip (depths of 4, 10, 20, 30, 40, and 50 km). In the variable locking tests, the deepest nodes were forced to be unlocked, the 3 nodes at the ends of each along-strike set of nodes were constrained to have the same ϕ value, and the seaward nodes at 4 and 10 km depth were constrained to be the same in the downdip direction but were allowed to vary along strike. This results in a total of 16 free node parameters. Convergence of the Juan de Fuca (JF) plate with NA is assumed to be the sum of JF-Pacific [*Wilson*, 1993] and Pacific-NA [*DeMets and Dixon*, 1999] poles and this pole was held fixed. All of the GPS sites shown in Fig. 8 are assumed to be on the Oregon block whose rotation pole relative to North America is estimated.

Solving for variable plate locking only (VL; 16 parameters) results in $\chi_v^2 = 9.64$ while the solution for rotation only (R; 3 parameters) gives $\chi_v^2 = 6.09$ (Table 1) which is significantly better at 99.97% level. Hence, the rotation of Oregon clearly accounts for more of the GPS signal than plate locking. Solving simultaneously for uniform plate locking and rotation results in an improved fit ($\chi_v^2 = 2.80$)

and allowing variable locking gives $\chi_v^2 = 1.51$. The probabilities are less than 10^{-5} that the VL, R, or UL-R models fit worse than the VL-R model by chance. Hence, both locking and rotation are needed to explain the Oregon GPS data. The predicted GPS vectors (Fig. 8b) provide an acceptable fit to the observations (χ^2 for the GPS is 1.38).

The resulting variable locking (slip deficit) model (Fig. 9a) is very similar to that produced by *McCaffrey et al*. [2000b] in that locking is largely offshore, there is a S to N increase in slip deficit, and there is a secondary downdip high in locking beneath central Oregon (Figs. 9a and 9c). The locked patch beneath land at 44°N is likely resulting from the gentler landward decay of strain rates at this latitude than to the north and south (Fig. 8a). As explained by *Williams and McCaffrey* [2001] we think the deeper locked zone may be due to the unrealistic stiffness of elastic half-space models and that these data can be fit with only offshore locking if a finite-thickness elastic 'plate' model is used.

Model VL_c-R, in which the locking on the subduction thrust is constrained to not increase in the downdip direction, distributes the local high in locking below the west-central Oregon forearc (Figs. 9b and 9d) and as expected produces a slightly higher misfit than model VL-R ($\chi_v^2 = 1.58$, the probability that it fits worse than VL-R simply by chance is high, 37%, indicating this is an acceptable model). This result suggests that the transition zone, as inferred from the dislocation model, is much broader beneath the central Oregon coast than it is to the north and south (Fig. 9d). This result is in contrast to *Hyndman and Wang* [1995] who felt the transition zone does not reach the coast at 44°N based largely on the lack of uplift rates at the coast (the tide gauge at the coast indicates 0.6 mm/a uplift). Model VL_c-R, which has instead a very gently tapered transition zone (Fig 9d), also predicts a low (0.1 mm/a) uplift rate at the coast at 44°N. In general, a broader transition zone than the one inferred by *Hyndman and Wang* [1995] is also indicated by the slow slip event beneath Washington and Vancouver Island in 1999 that ruptured entirely downdip of their transition zone [*Dragert et al*., 2001].

The pole of rotation for Oregon relative to North America (Fig. 8) is at 45.3±0.1°N, 241.5±0.1°E, and –0.79±0.04 °/Ma. This is about 1° SE of the pole estimated by *McCaffrey et al*. [2000b] but still within the bounds of the geologic pole of *Wells et al*. [1998]. The revised pole is based on data that is more certain and more widely distributed than was the *McCaffrey et al*. pole and is therefore more robust. At this point we cannot rule out that the extent of the rotating Oregon block includes all the GPS sites shown in Fig. 8. The north and northeast boundary of the block is probably the Olympic – Wallowa lineament (OWL; Fig. 8a) where contraction is evident in the geology [*Wells et al*., 1998]. The OWL extends to the NW into the Puget Lowlands of Washington State where permanent deformation (convergence) is predicted by the rotation pole to be about

5.0 ± 0.3 mm/a in a 41 ±1° azimuth. The SE boundary of the Oregon block is likely formed by Basin and Range extension which pushes Oregon to the NW. The southern boundary appears to be in northern California [*Wells et al*., 1998] but the GPS results here do not provide much information about that boundary.

Costa Rica

Across the Middle America trench (MAT) southwest of Costa Rica the Cocos plate converges with the Caribbean plate at about 88 mm/a [*DeMets*, 2001] with obliquity that increases from SE to NW (Fig. 10). *Lundgren et al.* [1999] (here called *L99*) presented GPS results from 1994 to 1997 and modeling for the Costa Rica section of the MAT. In SE Costa Rica convergence is nearly perpendicular to the MAT and the strain tensor derived from GPS (Table 2) is nearly uniaxial contraction (Fig. 10). In northern Costa Rica, where the Nicoya Peninsula juts out toward the trench, the oblique convergence appears to be partitioned. In the forearc the contraction direction is nearly uniaxial and normal to the Nicoya Peninsula. Near the volcanic arc the principal axes are rotated by about 30° and are consistent with right-lateral shear along the NW trend of the volcanic arc. The across-arc variation in the principal strain rates have a pattern that is reminiscent of Sumatra and suggests that slip partitioning occurs.

To account for motion of the forearc, *L99* assumed a fixed direction and rate of 7 mm/a based on unpublished modeling. Examination of the deflection of interplate earthquake slip vectors also suggest that the Costa Rica forearc moves along the arc on average at 7 mm/a [*McCaffrey*, 1996]. Moreover, in regions where obliquity changes along strike, margin-parallel stretching of the forearc is also common. Accordingly, in Costa Rica, the slip vectors indicate a margin-parallel stretching rate of 34±4 nanostrain/a [*McCaffrey*, 1996] while GPS results in the forearc give a reasonable agreement of 44±35 nanostrain/a (Table 2; Fig. 10).

Lundgren et al. [1999] performed inversions for interseismic plate coupling below the Nicoya Peninsula using all 3 components of their GPS results. They parameterized coupling on a planar thrust fault by dividing it into 56 coplanar 20x30 km rectangles and solved for slip deficit on each rectangle. They inferred a complex distribution of locking with an increased rate at the southern end of the Nicoya Peninsula. I represent the fault plane with 35 nodes (Fig. 11) distributed across the Nicoya Peninsula (NP) using depth contours reported by *L99* (6.0, 12.3, 25.9, 50.2, and 75.2 km). Unlike their fault model, I curve it to match the change in the trench orientation. For the variable locking model, the 35 nodes are grouped into 9 free parameters (Fig. 11b). Like *L99*, I take the boundary between the forearc and the Caribbean plate to fall along the volcanic arc (Fig. 11a) and I fix Cocos – Caribbean motion using the pole of *DeMets* [2001]. The 14 GPS vectors (3 components

each) and 26 earthquake slip vectors were used to solve for the forearc motion and plate coupling.

The VL and R models result in χ_v^2 of 1.61 and 1.96, respectively. (*Lundgren et al.* do not give statistics of their fits to compare.) Using uniform locking and rotation (UL-R) gives χ_v^2 = 1.24 while rotation and variable locking (VL-R; Fig. 11b) gives a fit, χ_v^2 = 0.77, which is better than the UL-R model at the 96% level. For Costa Rica the locking parameters alone explain the data better than the rotation alone but neither match the data as well as the combination (Table 1). Model VL_c-R (Fig. 11c) in which locking is variable but constrained to decrease downdip is not significantly different than model VL-R.

Spatial variations in locking appear to be required by the data indicated by the poorer fit of the UL-R model and by GPS velocities at the northern and southern ends of the NP that are considerably slower than in the center of it (Fig. 11a). These data indicate a patch of high locking beneath the central NP (Fig. 11b) which last had a M 7.5 in 1950 [*Lundgren et al*. 1999]. More recent large earthquakes have occurred north and south of this patch.

The rotation pole for the Costa Rica forearc is near 12°N, 277°E but the uncertainties in the pole location are quite large due to the small aperture of the GPS network. Using the local vertical axis rotation parameterization, the rigid block velocity at 10.5°N, 275°E is 5.8 ± 5.5 mm/a and the rotation rate is 0.04 °/Ma. This rate of forearc motion satisfies the earthquake slip vector azimuths within their errors (assumed to be 10°; Table 1). This velocity represents the slip rate across the volcanic arc, if that is where the slip between the forearc and the Caribbean plate occurs (Fig. 11a). It is half of the forearc slip rate that *DeMets* [2001] estimates for the MAT to the northwest which is consistent with the factor of two obliquity increase to the NW.

CONCLUSIONS

In this paper I outline a simple method to combine rigid body rotations of crustal blocks in either spherical or Cartesian systems with strain rates arising from the blocks interacting across faults at their boundaries. The approach is a merging of two conventional methods – using poles to describe motions of rotating spherical lithospheric plates and calculating surface deformation near faults with elastic halfspace dislocations. The combined approach allows one to utilize a greater variety of geophysical data types than in either approach alone. In particular, the method permits the use of GPS data for estimation of rigid block rotations in regions where significant strain rates occur due to nearby locked faults. It also allows estimations of plate locking parameters in regions where block rotations may produce complex velocity fields.

The method is applied briefly to Sumatra, Oregon, and Costa Rica where forearc blocks are suspected of being detached from the overriding plate. For all three examples, the

combination of rigid body rotation of the forearc and plate coupling on the subduction thrust is required to fit the observations. Fits to the data using plate coupling alone or rotation alone produce significantly poorer fits. Although I have focussed here on mobile forearcs, the method is applicable to other regions where multiple rotating blocks are expected such as in continental deformation zones.

APPENDIX

Recently, *Murray and Segall* [2001] incorporated block rotations in a spherical coordinate system with dislocation modeling and, by omission of appropriate citations, claim to be first to do so. However, to my knowledge, this approach of integrating rotations of spherical plates and fault strains by applying backslip along plate-bounding faults, as is described in detail in this paper, was first used by us to model the three-plate problem involving forearc motion and plate locking strain rates in Sumatra [*Prawirodirdjo et al*., 1997; hereafter called P97] using a computer program DEF-NODE developed and written by me [*McCaffrey*, 1995]. We used Euler poles to describe the relative motions of all plates - the Sumatran forearc, Australian plate, and Eurasian plate. Both the rigid-body block motions and the slip vectors across block-bounding faults were derived from the Euler poles. To account for interseismic strain accumulation, we applied the backslip method [*Savage*, 1983] along both the thrust and strike-slip faults (slip directions on faults were derived from the Euler poles also) using the *Okada* [1985] formulas and summed the surface velocities due to fault backslip with the velocities from the block rotations. While our description of the method in P97 was brief, as I show here, the presence of rotating crustal blocks is very clear in Figure 1 of that paper.

In Figure A1 I show the calculated curves from P97 that reveal forearc rotation. Because rotation produces non-zero velocity gradients $dV_x/dy = - dV_y/dx$, it should show up in the arc-normal profiles of the arc-parallel velocities (Fig. A1a) and in arc-parallel profiles of the arc-normal velocities (Fig. A1b). If one does not use an Euler pole to determine the forearc's motion, but instead translates the forearc, the calculated curves do not show the gradients that are clear in the P97 calculations (thick gray curves in Fig. A1). The numerical calculation where the forearc is translated along strike (no rotation) agrees very well, as it should, with the *Savage and Burford* [1973] analytical solution for a two-dimensional, Cartesian strike-slip fault (Fig. A1a) but does not match the P97 profile.

To estimate the effect of spherical rotations on such a profile, following *Savage and Burford* [1973], in the reference frame of the non-rotating block, the transverse (small circle) velocity along a profile that forms a great circle going through the Euler pole and crosses a vertical strike-slip fault forming a small circle about the pole is:

$$v(\Delta) = \omega R_e (\sin \Delta - \sin \Delta_f) H(\Delta - \Delta_f) + 0.5 v_f$$

$$+ v_f \pi^{-1} \arctan (R_e (\Delta - \Delta_f) / D) \qquad \text{(A1)}$$

where:
Δ is angular distance from the pole,
Δ_f is the distance of the fault from the pole,
ω is the angular velocity of the rotating block relative to the fixed block,
R_e is the Earth's radius,
H is the Heaviside function,
$v_f = \omega R_e \sin \Delta_f$ is the slip rate at the fault, and
D is the locking depth on the fault.

The first term is the rotational part of the block motion, the second term puts the solution into the reference frame of the non-rotating block, and the third is the screw dislocation approximation for the locked fault [*Savage and Burford*, 1973]. Applying this equation to the P97 northern Sumatra profile with $\Delta_f = 20.4°$, $\omega = 0.7°$/Ma, and D = 15 km (parameters taken from P97 model) gives the curve shown in Figure A1a. This agrees closely with the P97 profile indicating clearly that the P97 profile includes rotation of the forearc block. The small discrepancy at the SW end of the P97 profile is due to strain from locking on the subduction thrust fault that cannot be modeled with equation A1.

Acknowledgments. Reviews by Tim Dixon, Eryn Klosko, Jeff Freymueller, Alberto Lopez, and Bob Smalley were very helpful. Discussions about dislocation modeling with Smalley, Mike Bevis and Jim Savage are appreciated. GPS data from Oregon and Washington were made available by Jim Savage, Will Prescott, and Elliott Endo. Oregon continuous data are from the PANGA and NGS CORS arrays. Supported by NSF grant EAR-9814926 and USGS grant NEHRP-99HQGR0014

REFERENCES

Bevis, M., and S. J. Martel, Oblique plate convergence and interseismic strain accumulation, *Geochem. Geophys. Geosyst*., 2, 2001.

DeMets, C., A new estimate for present-day Cocos-Caribbean plate motion: Implications for slip along the Central American volcanic arc, *Geophys. Res. Letters*, 28, xxxx-xxxx, 2001.

DeMets, C., R. G. Gordon, D. F. Argus, and S. Stein, Effects of recent revisions to the geomagnetic reversal time scale on estimates of current plate motions, *Geophys. Res. Letters* 21, 2191-2194, 1994.

DeMets, C. and T. H. Dixon, New kinematic models for Pacific-North America motion from 3 Ma to present, I: Evidence for steady motion and biases in the NUVEL-1A model, *Geophys. Res. Letters*, 26,1921-1924, 1999.

Dragert, H., K. Wang, and T. S. James, A silent slip event on the deeper Cascadia subduction interface, *Science*, 292, 1525- 1528, 2001.

Fitch, T.J., Plate convergence, transcurrent faults and internal deformation adjacent to southeast Asia and the western Pacific, *J. Geophys. Res., 77*, 4432-4460, 1972.

Genrich, J. F., Y. Bock, R. McCaffrey, L. Prawirodirdjo, C. W. Stevens, S.S.O. Puntodewo, C. Subarya, and S. Wdowinski, Slip distribution at the northern Sumatra Fault System, *J. Geophys. Res*., 105, 28,327-28,341, 2000.

Hyndman, R. D., and K. Wang, The rupture zone of Cascadia great earthquakes from current deformation and the thermal regime, *J. Geophys. Res., 100*, 22133-22154, 1995.

Jarrard, R. D., Terrane motion by strike-slip faulting of forearc slivers, *Geology* 14, 780-783, 1986.

Lundgren, P., M. Protti, A. Donnellan, M. Heflin, E. Hernandez, and D. Jefferson, Seismic cycle and plate margin deformation in Costs Rica: GPS observations from 1994 to 1997, *J. Geophys. Res.*, 104, 28,915-28,926, 1999.

Mao, A., C. G. A. Harrison, and T. H. Dixon, Noise in GPS coordinate time series, *J. Geophys. Res*. 104, 2797-2816, 1999.

Matsu'ura, M., D. D. Jackson, and A. Cheng, Dislocation model for aseismic crustal deformation at Hollister, California, *J. Geophys. Res*. 91, 12661-12674, 1986.

McCaffrey, R., DEF-NODE users guide, Rensselaer Polytechnic Institute, Troy, 1995.

McCaffrey, R., Estimates of modern arc-parallel strain rates in fore arcs, *Geology* 24, 27-30, 1996.

McCaffrey, R., Active tectonics of southern Tibet: Oblique convergence, strain partitioning, and margin-parallel extension, *Eos, Trans AGU*, 80, 1999.

McCaffrey, R., P. Zwick, Y. Bock, L. Prawirodirdjo, J. Genrich, C. W. Stevens, S. S. O. Puntodewo, and C. Subarya, Strain partitioning during oblique plate convergence in northern Sumatra: Geodetic and seismologic constraints and numerical modeling, *J. Geophys. Res.*, 105, 28,363-28,376, 2000a.

McCaffrey, R., M. D. Long, C. Goldfinger, P. Zwick, J. Nabelek, C. K. Johnson and C. Smith, Rotation and plate locking along the southern Cascadia subduction zone, *Geophys Res. Letters*, 27, 3117-3120, 2000b.

McCluskey, S., et al., Present day kinematics of the eastern California Shear zone from a geodetically constrained block model, *Geophys. Res. Letters* 28, 3369-3372, 2001.

Meade, B. J., and B. H. Hager, Simultaneous inversions of geodetic and geologic data for block motions in plate boundary zones, *Eos, Trans AGU*, Paper G51B-16, 1999.

Miller, M. M., D. J. Johnson, C. M. Rubin, H. Dragert, K. Wang, A. Qamar, and C. Goldfinger, GPS-determination of along-strike variation in Cascadia margin kinematics: Implications for relative plate motion, subduction zone coupling, and permanent deformation, *Tectonics*, 20, 161-176, 2001.

Murray, M. H., and P. Segall, Modeling broadscale deformation in northern California and Nevada from plate motions and elastic strain accumulation, *Geophys. Res. Letters* 28, 4315-4318, 2001.

Newcomb, K. R., and W. R. McCann, Seismic history and seismotectonics of the Sunda Arc, *J. Geophys. Res.*, 92, 421-439, 1987.

Okada, Y., Surface deformation to shear and tensile faults in a half-space, *Bull. Seismol. Soc. Am.*, 75, 1135-1154, 1985.

Platt, J. P., Mechanics of oblique convergence, *J. Geophys. Res.* 98, 16239-16256, 1993.

Prawirodirdjo, L., Y. Bock, R. McCaffrey, J. Genrich, E. Calais, C. Stevens, S. S. O. Puntodewo, C. Subarya, J. Rais, P. Zwick, and Fauzi, Geodetic observations of interseismic strain segmentation at the Sumatra subduction zone, *Geophys. Res. Letters* 24, 2601-2604, 1997.

Press, W. H., B. P. Flannery, S. A. Teukolsky, and W. T. Vetterling, Numerical Recipes, Cambridge Univ. Press, Cambridge, 1989.

Savage, J. C., A dislocation model of strain accumulation and release at a subduction zone, *J. Geophys. Res.*, 88, 4984-4996, 1983.

Savage, J. C., Comment on "The stress state implied by dislocation models of subduction deformation" by J.J. Douglass and B. A. Buffet, *Geophys. Res. Letters* 23, 2709-2710, 1996

Savage, J.C., and M. Lisowski, Deformation in the Yakataga seismic gap, Southern Alaska, 1980-1986, *J. Geophys. Res.*, 93, 4731-4744, 1988.

Savage, J. C., J. L. Svarc, W.H. Prescott, and M. Murray, Deformation across the foraerc of the Cascadia subduction zone at Cape Blanco, Oregon, *J. Geophys. Res.,* 105, 3095-3102, 2000.

Savage, J.C., W. Gan, and J. L. Svarc, Strain accumulation and rotation in the eastern California shear zone, *J. Geophys. Res*. 106, 21,995-22,007, 2001.

Sella, G. F., T. H. Dixon, and A. Mao, REVEL: a model for recent plate velocities from space geodesy, J. Geophys. Res., 2001.

Sieh, K., S. N. Ward, D. Natawidjaja, and B. W. Suwargadi, Crustal deformation at the Sumatran subduction zone revealed by coral rings, *Geophys. Res. Letters*, 26, 3141-3144, 1999.

Sieh, K., and D. Natawidjaja, Neotectonics of the Sumatran fault, Indonesia, *J. Geophys. Res*. 105, 28,295, 2000.

Sillard, P., Z. Altamimi, and C. Boucher, The ITRF96 realization and its associated velocity field, *Geophys. Res. Lett*., 25, 3223-3226, 1998.

Snyder, J. P., Map Projections – A working manual, *U.S. Geological Survey Prof. Paper* 1395, pp. 383, 1987.

Stevens, C., R. McCaffrey, Y. Bock, J. Genrich, C. Vigny, C. Subarya, S.S.O. Puntodewo, and Fauzi, GPS evidence for rapid rotations about a vertical axis in a collisional setting: the Palu fault of Sulawesi, Indonesia, *Geophys. Res. Letters*, 26, 2677-2680, 1999.

Tichelaar, B. W., and L. J. Ruff, Depth of seismic coupling along subduction zones*, J. Geophys. Res., 98*, 2017-2037, 1993.

Wallace, L., et al., Edge-driven block rotations interpreted from new GPS results: Papua New Guinea, *Eos Trans. AGU*, 2001.

Wells, R. E., C. S. Weaver, and R. J. Blakely, Forearc migration in Cascadia and its neotectonic significance, *Geology*, 26, 759-762, 1998.

Williams, C. A. and R. McCaffrey, Stress rates in the central Cascadia subduction zone inferred from an elastic plate model, *Geophys. Res. Lett*., 28, 2125-2128, 2001.

Williams, C. A., R. McCaffrey, and A. Qamar, Inversions of geodetic data for rotation pole and deformation mechanism at subduction zones: Applications to Cascadia, Sumatra, and Alaska, *Eos Trans. AGU*, 2001.

Wilson, D. S., Confidence intervals for motion and deformation of the Juan de Fuca plate, *J. Geophys. Res. 98,* 16,053-16,071, 1993.

Robert McCaffrey, Department of Earth and Environmental Sciences, Rensselaer Polytechnic Institute, Troy, NY 12180 USA

Figure 1. (a) Example of a three-plate system. Each plate's motion is described by a pole of rotation relative to a common reference frame. The relative motions across the faults that separate the plates are determined by the differences in the block velocities predicted by these poles. The velocity field for the region is the sum of the block rotations and the velocities arising from locking on faults. (b) Three-plate system used to test the impact of obliquity, plate coupling, and slip partitioning on the obliquity of surface velocities in the upper plate. The vector ${}_{S}V_{O}$ shows the convergence of the subducting plate S relative to the major overriding plate O. ${}_{S}V_{F}$ shows the convergence of the subducting plate with the forearc F and becomes more normal to the trench as slip partitioning (SP) increases. This geometry was used to generate the plots in Figure 3.

Figure 2. (a) Illustration of nodes used to represent fault surface geometry and how slip is integrated across a fault. Node positions are specified along contours of the fault surface and their geographic positions are selected to keep the trapezoids between any 4 adjacent nodes as close to rectangular as possible while following the curvature of the fault. Slip at each node is specified or estimated by inversion and the area between nodes is divided into smaller patches. Slip at each patch is determined by linear (pyramidical) interpolation between the nodes and the surface deformation is calculated by summing the effects of each patch. (b) Surface response functions for slip at a node are calculated by applying at the node a unit slip which decreases linearly to zero at each adjacent node. Slip is integrated over the four trapezoids that touch the central node to estimate the surface deformation at each observation point. The surface deformation for any amount of slip at the node can then be determined by simple multiplication of the slip amount with this unit response. (c) Examples of the slip distributions on the fault surface for some groups of non-zero nodes.

Figure 3. Examples of surface velocities and strain rates when varying amounts of both slip partitioning and plate coupling occur, using the geometry of Figure 1b. (a) Profiles of surface velocity components and obliquities for varying fractions of slip partitioning (SP) and depths of interplate coupling (DC). The subducting plate converges at an angle of 45° to the trench. Forearc slip is assumed to occur along a vertical strike-slip fault 300 km from and parallel to the trench – the strike-slip fault is locked to 15 km depth in each trial. For 0% SP the strike-slip fault does not slip, for 50% SP it slips at half the margin-parallel rate of relative plate motion (i.e., ½ of the margin parallel component of ${}_{S}V_{O}$ in Fig. 1b), and for 100% SP it moves at the full margin parallel component of ${}_{S}V_{O.}$ The thrust fault dips toward and under the forearc at 20° starting at $x = 0$ (labeled Trench). It is assumed to be fully coupled to the overriding plate to a depth given by DC (distance shown by the thick vertical line) and then coupling tapers to zero over the next 10 km of depth. These trials indicate that an increase in surface velocity obliquity is expected between the downdip end of coupling and the strike-slip fault when partitioning occurs. (b) Map views of predicted surface velocities for the corresponding trials in (a). (c) Map views of principal strain rates for the same trials.

Figure 4. (a) Illustration of the thrust fault in cross-section showing locked and unlocked patches used by *Bevis and Martel* [2001] to infer that large surface velocity obliquity anomalies can occur in the absence of slip partitioning. (b) Detail of the leading wedge of the overriding plate. (c) Surface velocities and obliquities from the *Bevis and Martel* [2001] model. The variation in the two horizontal velocity components due to including the unlocked patch near the trench (shown by gray bar) results in obliquities reaching twice their expected value (here 25°). (d) If the thrust fault does not include the free-slip section near the trench, the trench-parallel velocities on the surface of the wedge are more uniform, consistent with low strain rates in the wedge, and the expected obliquity anomaly is much smaller. (e) Tapering downdip edge of the locked zone decreases the obliquity anomaly even further.

Figure 5. (a) GPS vectors in central Sumatra shown relative to Eurasia with 1-sigma error ellipses. Thick vectors at trench are predicted Australia - Eurasia motion from NUVEL-1A [*DeMets et al*., 1994]. Opposing arrows show principle strain rates calculated from the GPS results for the rectangular regions shown by the boxes. IFZ = Investigator Fracture Zone. Triangles represent volcanoes. (b) GPS vector residuals (arrows with 1-sigma error ellipses) for model VL-R. Short thick arrows show observed slip vector and transform fault azimuths and thinner arrows are predicted azimuths. Vector with shaded error ellipse near 0°N, 100°E shows the rigid motion of the forearc block (FA) relative to the backarc (EUR) estimated at that point.

Figure 6. Profiles of surface velocity obliquities estimated from Sumatra GPS vectors. Obliquity is the angle the vector makes with N55°E, the approximate normal to the Java trench. Heavy line shows the approximate obliquity of convergence of Australian plate with Eurasia. Triangles show where the volcanic arc crosses the profile and SF shows where the Sumatra fault falls in the profile. In the north, the GPS obliquities appear to be systematically higher than plate obliquity, suggesting slip partitioning takes place as shown in Figure 3.

Figure 7. Coupling model VL-R for the subduction thrust off central Sumatra (see Table 1). Gray scale shows estimated slip deficit rate in mm/a. Numbered, black dots are nodes that outline the fault planes (numbers refer to their parameter index, any with the same index were constrained to have the same value of ϕ). Nodes along the Sumatra fault were all constrained to have the same coupling parameter value. Triangles are GPS observation points and inverted triangles are uplift rate observation points. Heavy black lines show the outline of the forearc block used in the inversion. Plus symbols "+" are every degree of latitude and longitude.

Figure 8. (a) Oregon region showing tectonic features and GPS vectors relative to North America with 1-sigma error ellipses. Vectors west of trench line show predicted Juan de Fuca - North America motion. Opposing arrows show principal strain rates calculated from the GPS results for the rectangular regions shown by the boxes. OWL = Olympic –Wallowa lineament. Triangles represent volcanoes. (b) Residual (observed minus predicted) GPS vectors for model VL-R. The estimated Oregon – North America pole of rotation with 1-sigma ellipse is shown in NE Oregon.

Figure 9. Coupling models VL-R and VL_c-R (Table 1) for the Cascadia subduction zone in Oregon. Numbered, black dots in (a) and (b) are nodes that outline the fault plane (numbers refer to their parameter index, any with the same index were constrained to have the same value of ϕ). Gray scale shows distribution of slip rate deficit ϕV in mm/a – this is the amount of slip rate that goes into locking at the plate interface. Triangles are GPS observation points and inverted triangles are uplift rate (tide gauge) observation points. Plus symbols "+" are every degree of latitude and longitude. (c) and (d) show the down-dip variation in slip deficit ϕV for three west to east profiles across the locking model at 42°N, 44°N, and 46°N, as labeled. Small gray bars show where the profiles intersect the coast. Model VL_c-R (b and d) differs from VL-R (a and c) in that the locking parameter ϕ was constrained to not increase in the downdip direction. This has the effect of distributing the coupling zone beneath west-central Oregon.

Figure 10. Costa Rica region showing tectonic features and GPS results from *Lundgren et al*. [1999] relative to the Caribbean plate. Vectors at trench line are predicted Cocos - Caribbean motion [*DeMets*, 2001]. Opposing arrows show principle strain rates calculated from the GPS results for the rectangular regions shown by the boxes. Triangles represent volcanoes.

Figure 11. (a) Observed and predicted GPS vectors for the Nicoya Peninsula region of Costa Rica for model VL-R (Table 1). Vectors that end in center of error ellipse (2.5-sigma) are observed GPS; long vectors originating at same points are calculated GPS; short NW-trending vectors at same points show the component of forearc motion due to rigid-body rotation. Other short arrows show observed and predicted earthquake slip vector azimuths in the forearc. Line through volcanic arc is the forearc northern block boundary block. Vector with shaded error ellipse near 10.5°N, 275°E shows the rigid motion of the forearc block relative to the backarc (Caribbean plate) estimated at that point. (b) Coupling model VL-R for the Nicoya Peninsula region of Costa Rica. Numbered, black dots are nodes that outline the thrust fault geometry (numbers refer to their parameter index, any with the same index were constrained to have the same value of ϕ). Gray scale shows resulting slip deficit rate in mm/a – this is the amount of subduction that goes into locking at the plate interface. Triangles show three-component GPS observation points. Plus symbols "+" are every degree of latitude and longitude. NP = Nicoya Peninsula; MAT = Middle America trench. (c) Model VL_c-R in which ϕ was constrained to not increase in the downdip direction.

Figure A1. (a) Cross-arc profile of arc-parallel velocities calculated in three ways and compared to the calculated curve (heavy line) of *Prawirdijiro et al*. [1997]. Calculated profiles that do not include an Euler rotation of the forearc do not match the *Prawirdijiro et al*. [1997] profile whereas the curve derived from equation A1, which includes rotation, matches well. (b) Along-strike profile of the arc-normal velocities in the forearc also show that forearc rotation is required to match the *Prawirdijiro et al*. [1997] profile. Velocities are relative to Eurasia. The Australia – Eurasia pole used is 24.4°N, 17.7°E, ω = 0.51°/Ma and the forearc – Eurasia pole is 12.0°N, 117.0°E, ω = -0.7°/Ma. See *Prawirdijiro et al*. [1997] for more details of the model and profiles.

Table 1. Results of inversions for locking and rotation models.

Region	Model	N_{GPS}	f	χ^2_{GPS}	N_{az}	σ_{az}	χ^2_{az}	N_{up}	f	χ^2_{up}	χ^2	N_{data}	N_P	DOF	χ_v^2	Prob.
Sumatra	VL	108	2	4.45	44[#]	15	2.57	10	5	6.10	654.3	162	14	148	4.421	0.000066
	R			9.06			2.91			*	1106.8	152	3	149	7.428	0.000000
	UL-R			4.48			0.83			19.42	714.4	162	5	157	4.550	0.000027
	VL-R			2.30			0.99			4.34	335.6	162	18	144	2.331	
	VL-R_c			3.93			3.11			4.51	606.7	162	15	147	4.127	0.000320
Oregon	VL	234	2	9.18				7	3	2.96	2169.4	241	16	225	9.642	0.000000
	R			6.01						*	1407.2	234	3	231	6.092	0.000000
	UL-R			2.66						6.09	664.6	241	4	237	2.804	0.000002
	VL-R			1.37						2.03	335.2	241	19	222	1.510	
	VL_c-R			1.43						2.27	351.0	241	19	222	1.581	0.365901
Costa Rica	VL	28	2	1.87	26	10	1.12	14	2	0.97	95.0	68	9	59	1.610	0.003032
	R			2.68			0.95			*	99.8	54	3	51	1.957	0.000386
	UL-R			1.64			0.97			0.57	79.3	68	4	64	1.239	0.035242
	VL-R			0.52			0.87			0.41	43.1	68	12	56	0.770	
	VL_c-R			0.84			0.94			0.47	54.5	68	12	56	0.973	0.191283

Models: VL = variable locking; R = rotation; UL = uniform locking; VL_c = variable locking with constraints; R_c = rotation pole constrained. N_{GPS} = number of GPS observations (N and E velocities are treated as separate observations). f = factor multiplied by formal standard deviation for weighting. N_{az} = number of slip vector and transform fault azimuths. σ_{az}- azimuth uncertainty. N_{up} = number of uplift rates. χ^2 with data type subscript are χ^2 divided by the number of observations for particular data type. χ^2 without subscript is total χ^2 for model. N_{data} = total number of observations. N_P = number of free parameters. DOF = degrees of freedom (number of observations minus the number of free parameters). χ_v^2 is the reduced chi-square, e.g., total χ^2 divided by DOF. [*]Uplift rate data were not used when solving for rotation pole only. [#]Includes 15 Sumatra fault azimuths. Prob. is the probability that this model fits the data worse than the corresponding VL-R model by random chance (F-test).

Table 2. Principal strain rates.

Latitude	Longitude	Tectonic	ε_1	α_1	ε_2	θ	DOF	χ_ν^2
°N	°E	Setting	nanostrain/a	degrees	nanostrain/a	nanoradians/a		
Sumatra								
-1.50	99.88	FA	-168±70	68±12	-81±31	-19±32	12	3.84
0.41	98.53	FA	-69±54	49±11	35±49	26±40	8	0.59
1.92	97.55	FA	-124±75	46±10	71±55	13±48	10	0.64
-0.37	100.54	A	-110±24	20±8	84±50	98±24	70	1.58
1.12	99.57	A	-73±24	11±11	52±49	68±27	22	1.28
2.62	98.71	A	-129±33	9±9	107±79	132±41	64	0.69
0.89	100.78	BA	-41±21	179±12	27±55	19±22	14	0.66
Oregon								
42.75	236.10	FA	-87±7	74±4	0±7	34±6	24	1.61
44.35	236.30	FA	-56±6	80±4	3±5	21±4	36	1.55
45.68	236.50	FA	-65±6	84±3	7±4	26±3	32	0.66
46.60	236.35	FA	-71±5	72±3	-7±4	24±3	36	1.24
42.80	237.50	A	-6±6	36±12	7±8	26±5	18	0.55
44.30	237.55	A	-27±8	77±10	-4±6	18±5	18	0.48
45.65	237.65	A	-10±9	86±11	8±6	19±5	20	1.07
46.60	237.75	A	-16±7	54±12	-2±6	13±5	22	0.71
42.85	239.05	BA	-25±8	141±11	-5±8	16±6	8	1.01
44.25	239.00	BA	-9±11	102±12	8±13	4±8	10	0.50
45.60	238.95	BA	-12±12	82±13	-8±15	31±9	12	1.34
46.70	239.65	BA	-40±14	80±9	27±20	-6±13	4	1.85
Costa Rica								
9.08	277.10	FA	-203±84	50±10	12±50	64±46	6	1.49
10.0	274.60	FA	-175±33	44±4	44±35	-20±25	16	2.21
10.63	274.95	A	-63±35	13±9	90±45	58±31	6	0.58

Latitudes and longitudes are given for the mid-point of the rectangular box containing the GPS points used for the horizontal strain calculation. Tectonic settings are: FA = forearc, A = volcanic arc, BA = backarc. α_1 = azimuth of principal axis whose magnitude is ε_1. Contraction is negative, extension is positive. Positive rotation rate is clockwise when viewed from above. 1 °/Ma ≈ 17.5 nanoradians/a. DOF = degrees of freedom (number of observations minus 6, the number of free parameters). χ_ν^2 is the reduced chi-square misfit.

Running heads:

BLOCK ROTATIONS AND PLATE COUPLING

ROBERT McCAFFREY

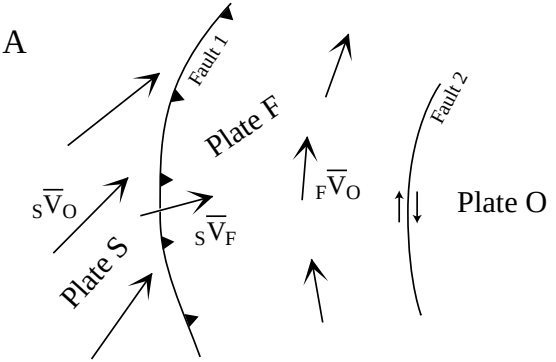
A
Fault 1
Plate F
Fault 2
Plate O
Plate S
$_S\overline{V}_O$
$_S\overline{V}_F$
$_F\overline{V}_O$

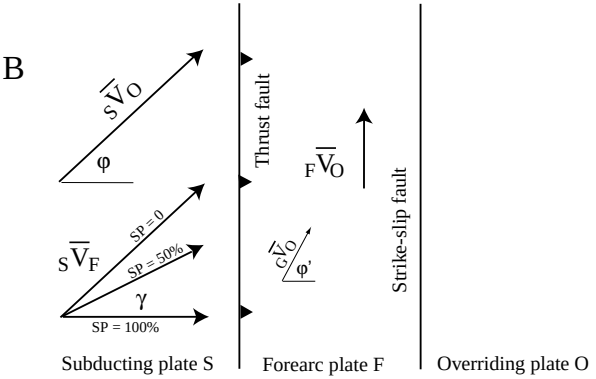
B
$_S\overline{V}_O$
φ
Thrust fault
$_F\overline{V}_O$
$_S\overline{V}_F$
SP = 0
SP = 50%
γ
SP = 100%
$_G\overline{V}_O$
φ'
Strike-slip fault
Subducting plate S
Forearc plate F
Overriding plate O

Fig. 1

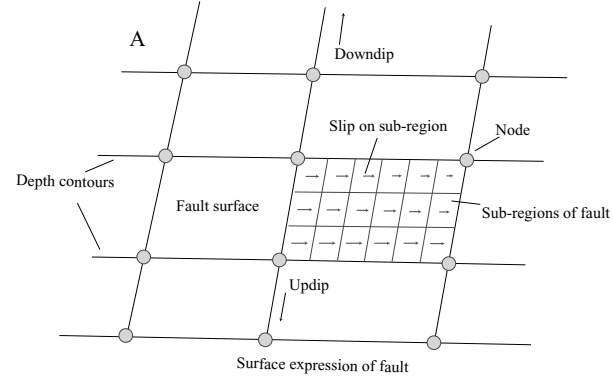
A
Downdip
Slip on sub-region
Node
Depth contours
Fault surface
Sub-regions of fault
Updip
Surface expression of fault

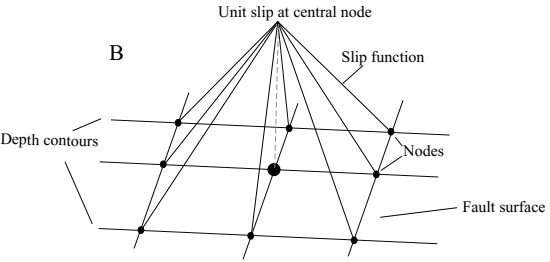
Unit slip at central node
B
Slip function
Depth contours
Nodes
Fault surface

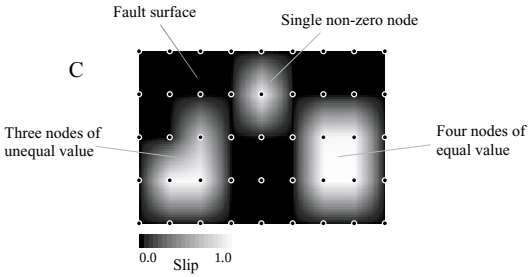
Fault surface
Single non-zero node
C
Three nodes of unequal value
Four nodes of equal value
0.0
Slip
1.0

Fig. 2

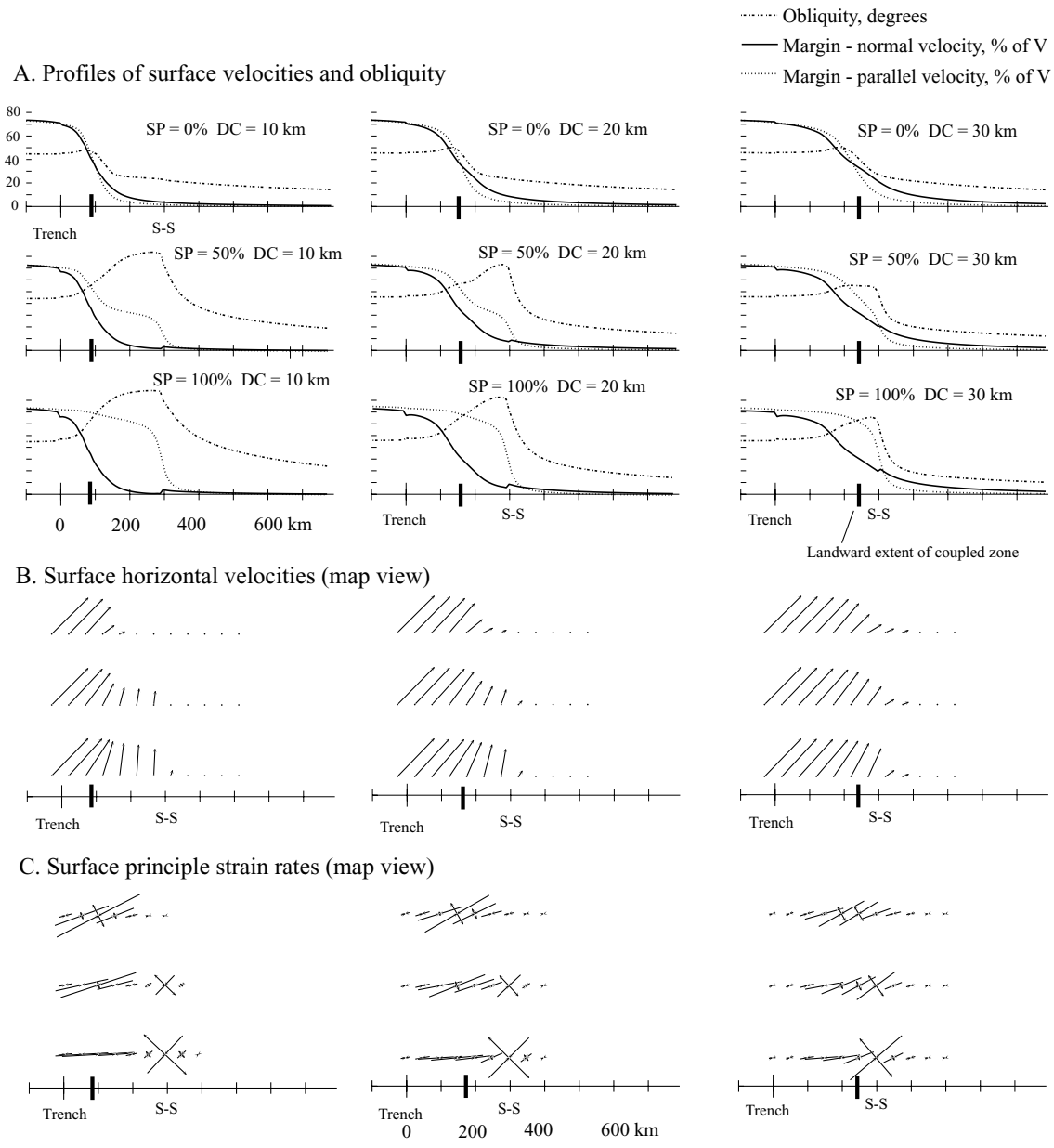
Obliquity, degrees
Margin - normal velocity, % of V
Margin - parallel velocity, % of V
A. Profiles of surface velocities and obliquity
80
60
40
20
0
SP = 0% DC = 10 km
SP = 0% DC = 20 km
SP = 0% DC = 30 km
Trench
S-S
SP = 50% DC = 10 km
SP = 50% DC = 20 km
SP = 50% DC = 30 km
SP = 100% DC = 10 km
SP = 100% DC = 20 km
SP = 100% DC = 30 km
0
200
400
600 km
Trench
S-S
Trench
S-S
Landward extent of coupled zone
B. Surface horizontal velocities (map view)
Trench
S-S
Trench
S-S
Trench
S-S
C. Surface principle strain rates (map view)
Trench
S-S
Trench
S-S
0
200
400
600 km
Trench
S-S

Figure 3

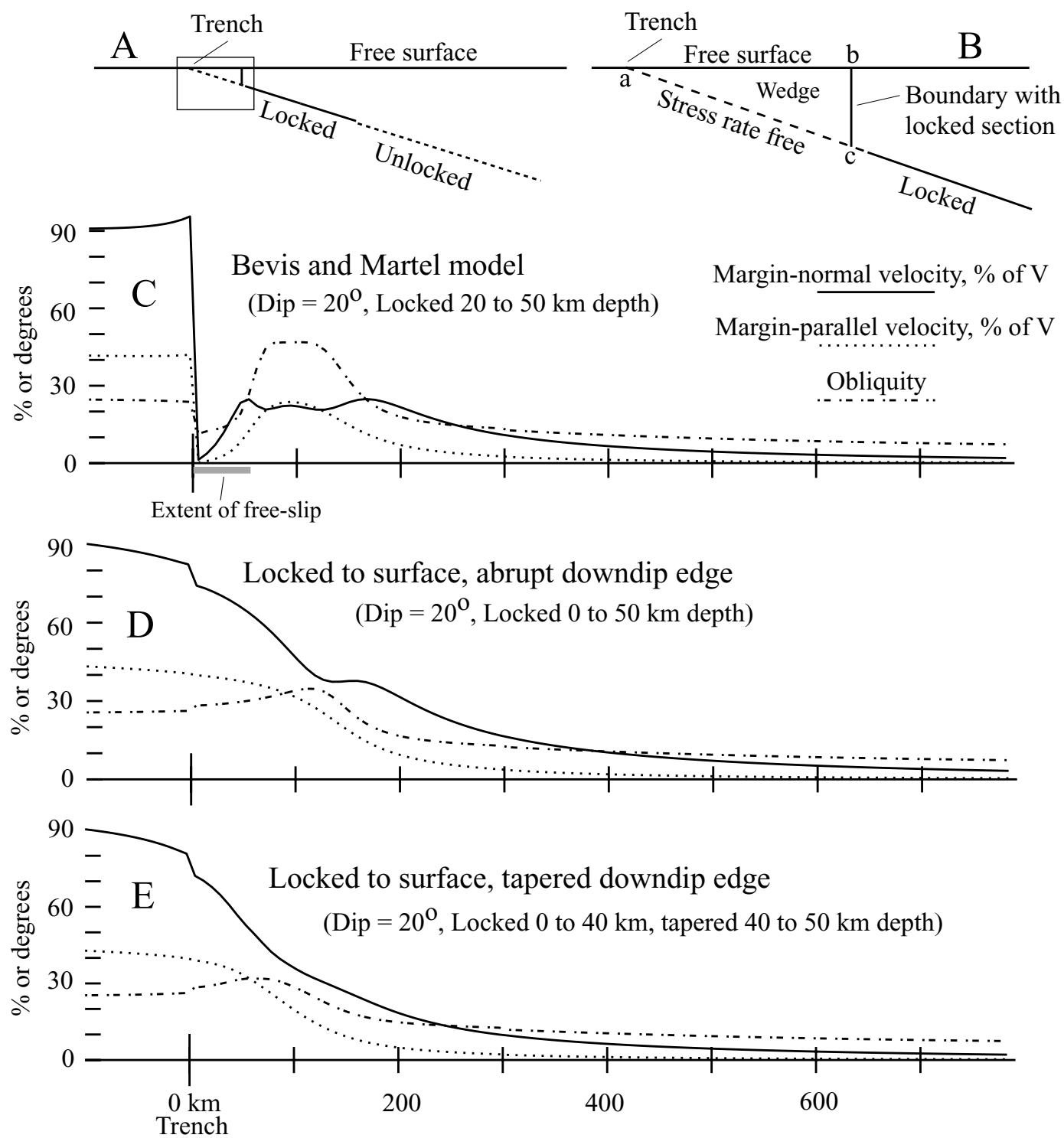
A
Trench
Free surface
Locked
Unlocked
B
Trench
Free surface
b
a
Wedge
Stress rate free
Boundary with
locked section
c
Locked
C
Bevis and Martel model
(Dip = 20°, Locked 20 to 50 km depth)
Margin-normal velocity, % of V
Margin-parallel velocity, % of V
Obliquity
% or degrees
90
60
30
0
Extent of free-slip
D
Locked to surface, abrupt downdip edge
(Dip = 20°, Locked 0 to 50 km depth)
E
Locked to surface, tapered downdip edge
(Dip = 20°, Locked 0 to 40 km, tapered 40 to 50 km depth)
0 km
Trench
200
400
600

Figure 4

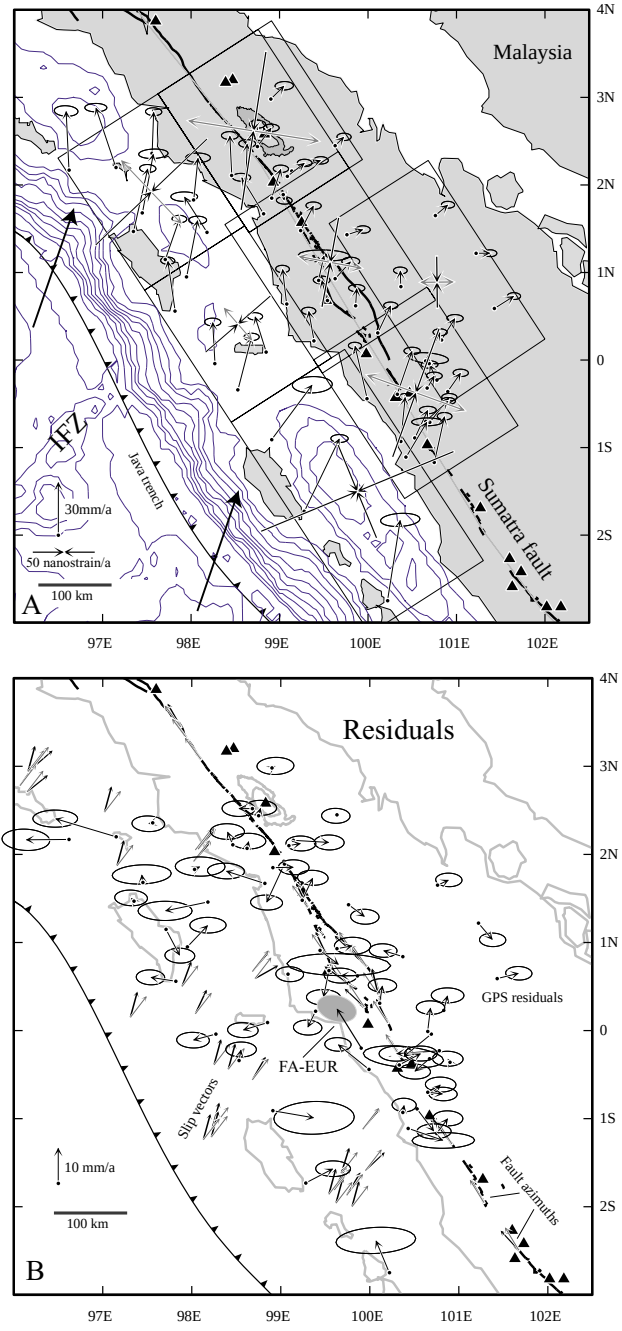
Malaysia
IFZ
Java trench
Sumatra fault
30mm/a
50 nanostrain/a
100 km
A
4N
3N
2N
1N
0
1S
2S
97E
98E
99E
100E
101E
102E

Residuals
GPS residuals
FA-EUR
Slip vectors
Fault azimuths
10 mm/a
100 km
B
4N
3N
2N
1N
0
1S
2S
97E
98E
99E
100E
101E
102E

Fig. 5

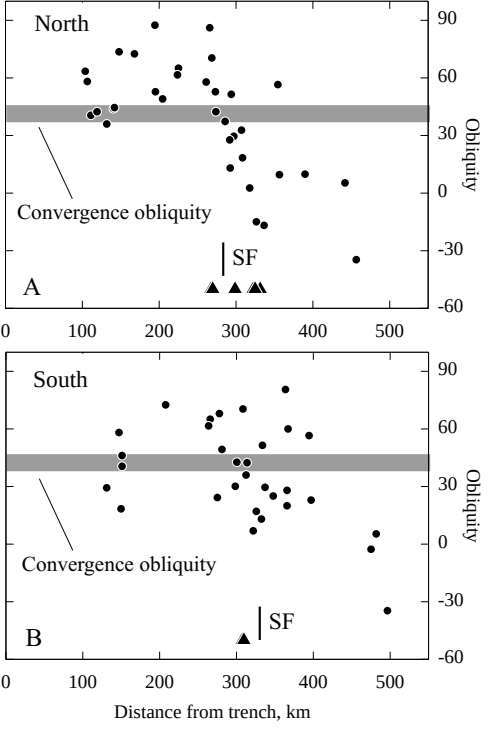
North
Convergence obliquity
SF
A
South
Convergence obliquity
SF
B
Obliquity
90
60
30
0
-30
-60
0
100
200
300
400
500
Distance from trench, km

Figure 6

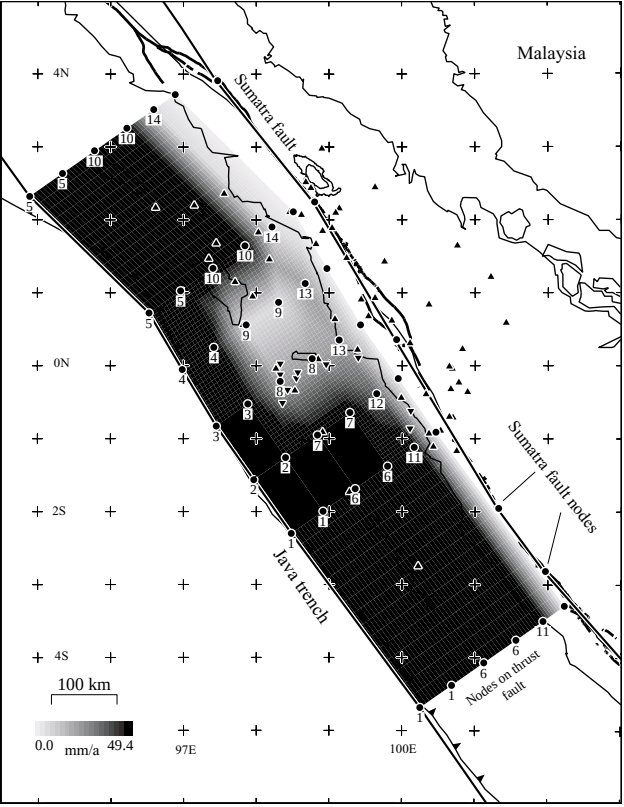
Malaysia
Sumatra fault
Sumatra fault nodes
Java trench
Nodes on thrust fault
4N
0N
2S
4S
97E
100E
100 km
0.0 mm/a 49.4

Fig. 7

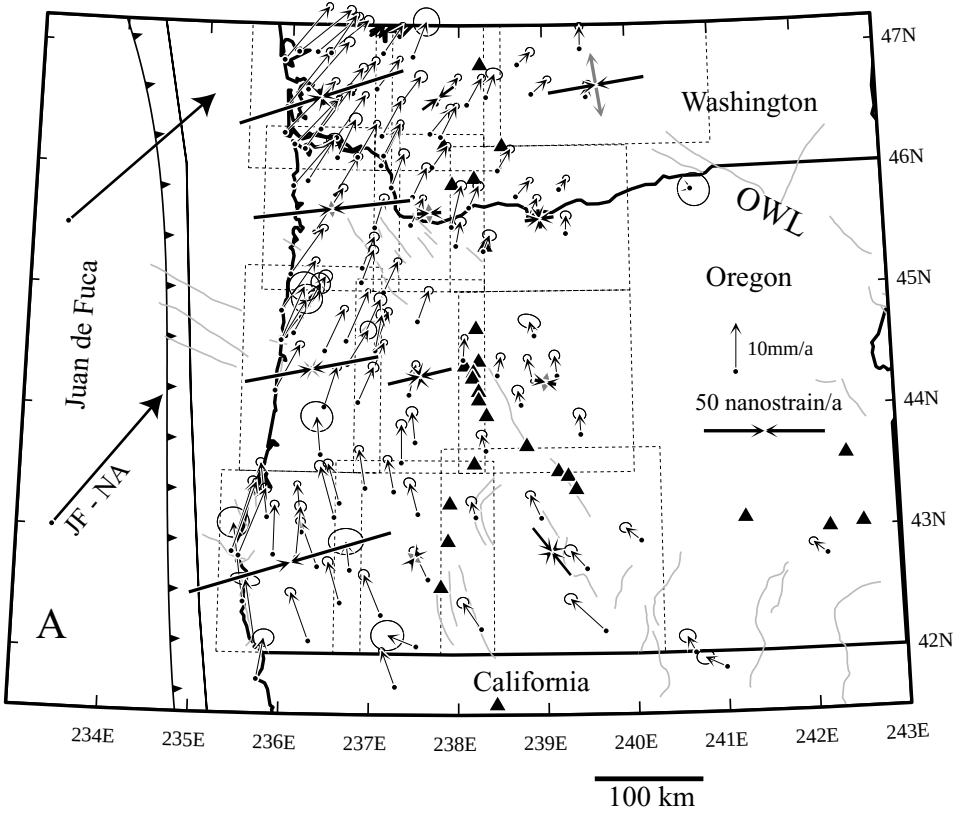
Washington
OWL
Oregon
Juan de Fuca
JF - NA
10mm/a
50 nanostrain/a
A
California
47N
46N
45N
44N
43N
42N
234E
235E
236E
237E
238E
239E
240E
241E
242E
243E
100 km

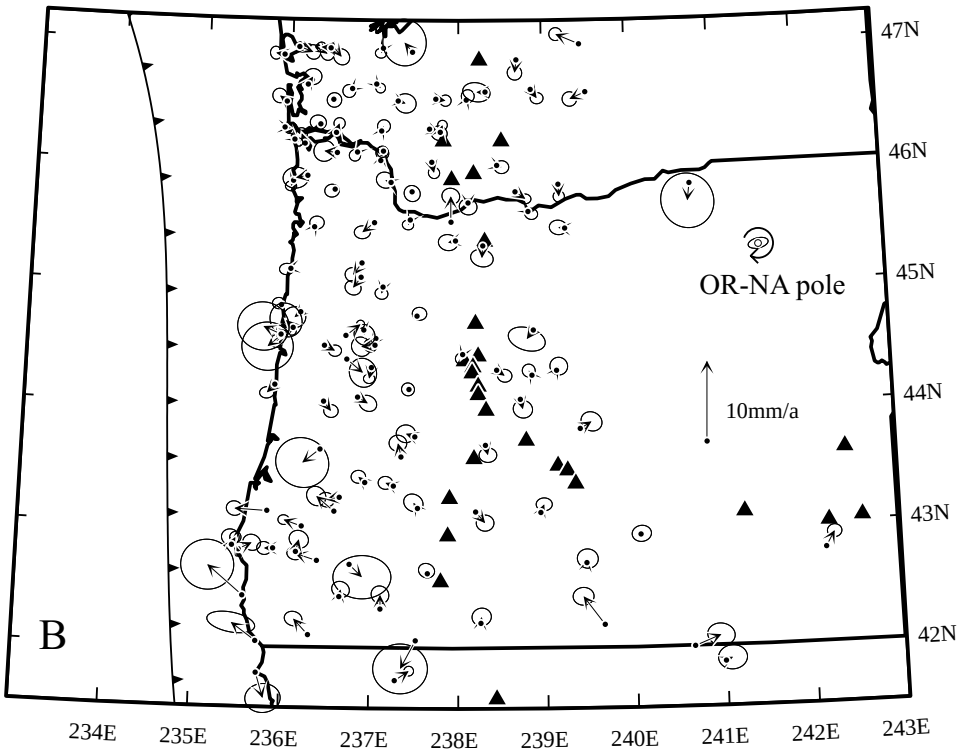
OR-NA pole
10mm/a
B
47N
46N
45N
44N
43N
42N
234E
235E
236E
237E
238E
239E
240E
241E
242E
243E

Fig. 8

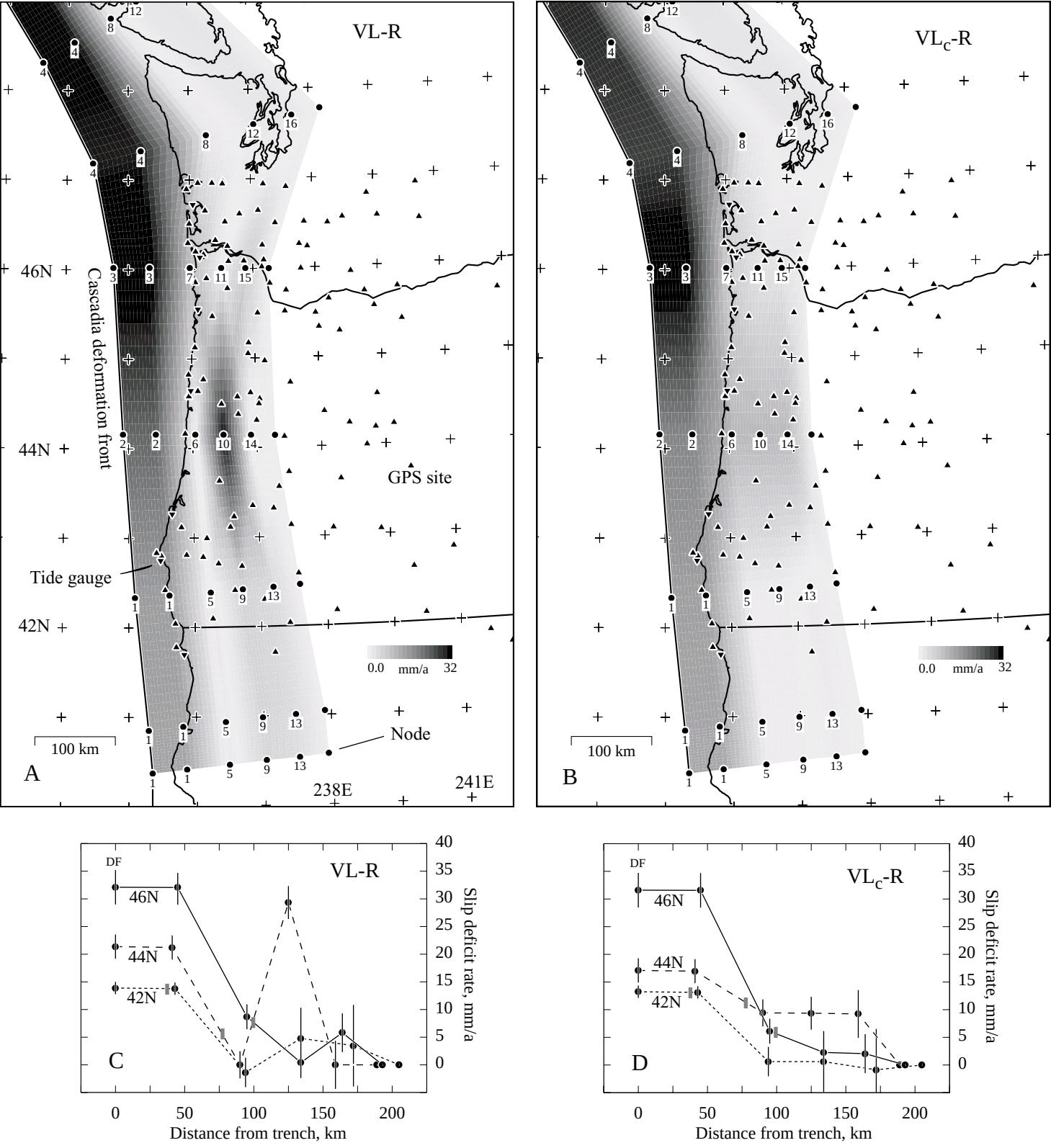
VL-R
VL$_c$-R
46N
44N
42N
Cascadia deformation front
GPS site
Tide gauge
Node
100 km
0.0 mm/a 32
238E
241E
A
B
DF
46N
44N
42N
C
D
Slip deficit rate, mm/a
Distance from trench, km
0
50
100
150
200
0
5
10
15
20
25
30
35
40

Fig. 9

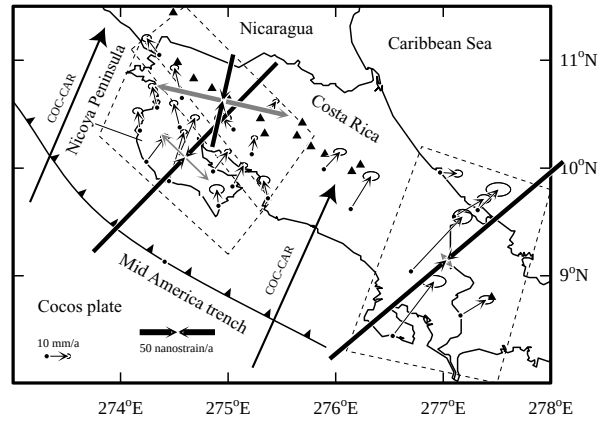
Nicaragua
Caribbean Sea
Nicoya Peninsula
COC-CAR
Costa Rica
Mid America trench
COC-CAR
Cocos plate
10 mm/a
50 nanostrain/a
11°N
10°N
9°N
274°E
275°E
276°E
277°E
278°E

Fig. 10

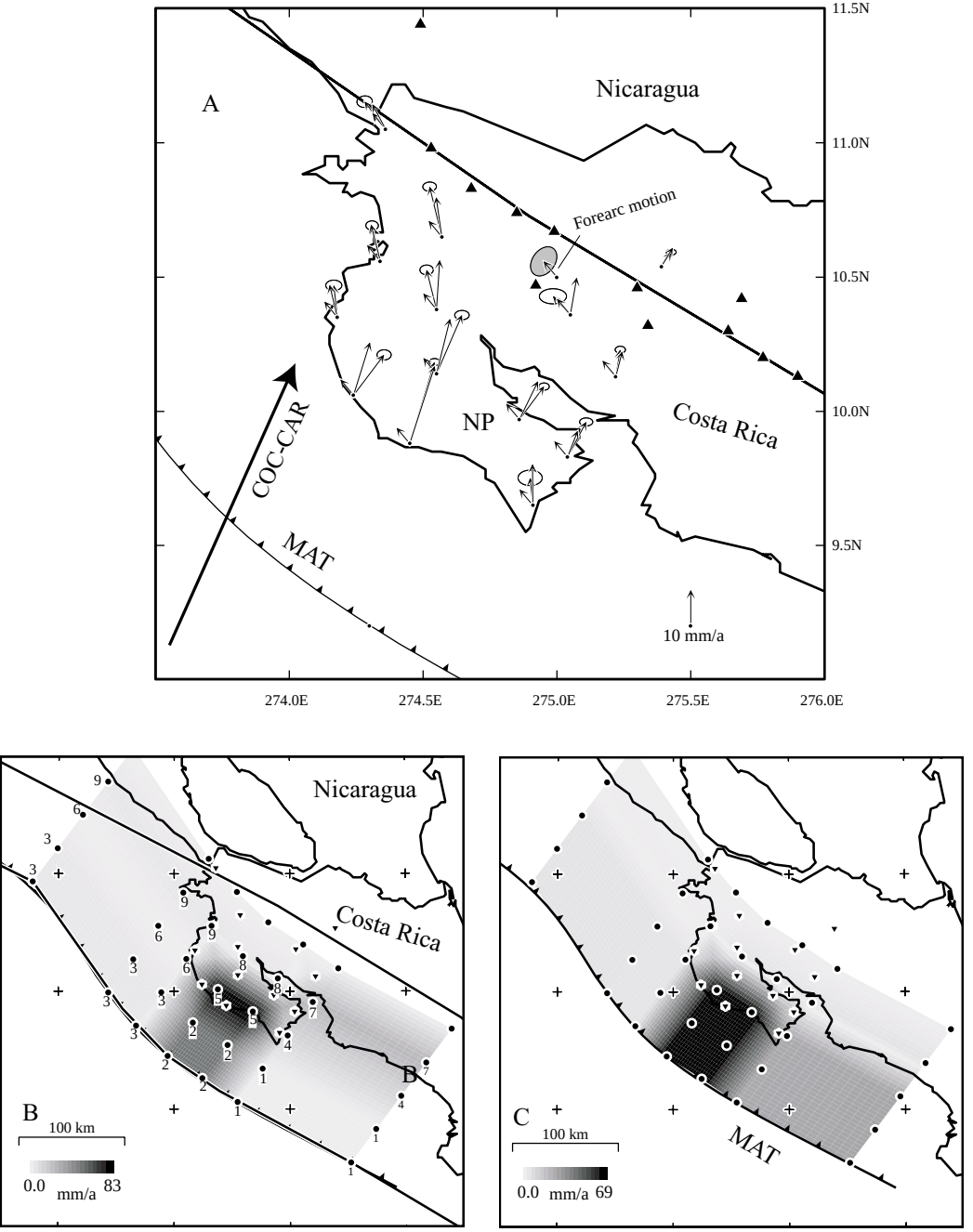
A
Nicaragua
Forearc motion
NP
Costa Rica
COC-CAR
MAT
10 mm/a
11.5N
11.0N
10.5N
10.0N
9.5N
274.0E
274.5E
275.0E
275.5E
276.0E
B
Nicaragua
Costa Rica
100 km
0.0 mm/a 83
C
100 km
MAT
0.0 mm/a 69

Fig. 11

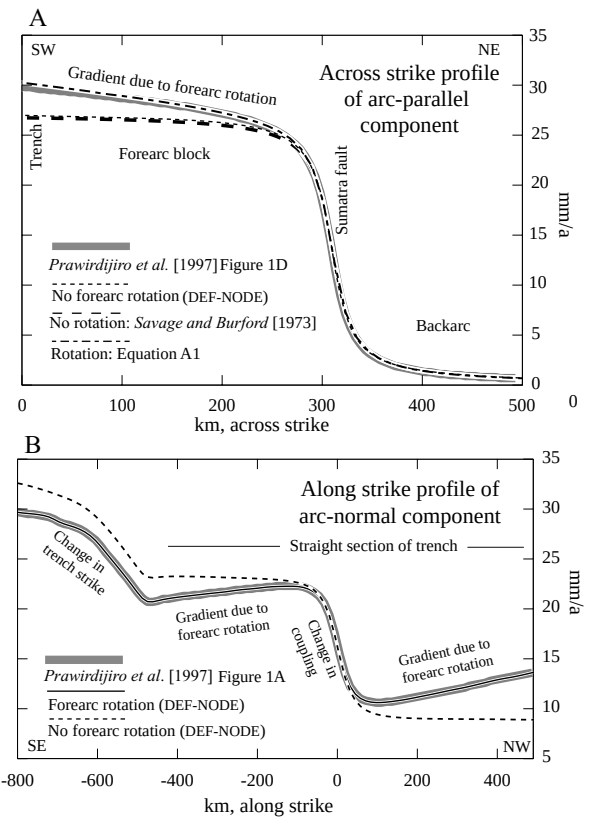
A
SW
NE
Gradient due to forearc rotation
Across strike profile of arc-parallel component
Trench
Forearc block
Sumatra fault
Backarc
mm/a
Prawirdijiro et al. [1997] Figure 1D
No forearc rotation (DEF-NODE)
No rotation: Savage and Burford [1973]
Rotation: Equation A1
0
100
200
300
400
500
km, across strike
B
Along strike profile of arc-normal component
Straight section of trench
Change in trench strike
Gradient due to forearc rotation
Change in coupling
Gradient due to forearc rotation
mm/a
Prawirdijiro et al. [1997] Figure 1A
Forearc rotation (DEF-NODE)
No forearc rotation (DEF-NODE)
SE
NW
-800
-600
-400
-200
0
200
400
km, along strike

Figure A1